

Topological quantum properties of chiral crystals

Guoqing Chang^{1,2,3,4,12}, Benjamin J. Wieder^{1,5,6,7,12}, Frank Schindler^{8,12}, Daniel S. Sanchez¹, Ilya Belopolski¹, Shin-Ming Huang^{1,9}, Bahadur Singh^{1,2,3}, Di Wu^{2,3}, Tay-Rong Chang¹⁰, Titus Neupert^{1,8}, Su-Yang Xu^{1*}, Hsin Lin^{2,3,4*} and M. Zahid Hasan^{1,11*}

Chiral crystals are materials with a lattice structure that has a well-defined handedness due to the lack of inversion, mirror or other roto-inversion symmetries. Although it has been shown that the presence of crystalline symmetries can protect topological band crossings, the topological electronic properties of chiral crystals remain largely uncharacterized. Here we show that Kramers–Weyl fermions are a universal topological electronic property of all non-magnetic chiral crystals with spin-orbit coupling and are guaranteed by structural chirality, lattice translation and time-reversal symmetry. Unlike conventional Weyl fermions, they appear at time-reversal-invariant momenta. We identify representative chiral materials in 33 of the 65 chiral space groups in which Kramers–Weyl fermions are relevant to the low-energy physics. We determine that all point-like nodal degeneracies in non-magnetic chiral crystals with relevant spin-orbit coupling carry non-trivial Chern numbers. Kramers–Weyl materials can exhibit a monopole-like electron spin texture and topologically non-trivial bulk Fermi surfaces over an unusually large energy window.

The spatial structures of three-dimensional crystal lattices are characterized by a finite set of possible symmetries that give rise to the 230 space groups (SGs) for non-magnetic materials^{1,2}. In this work, we examine the properties of the SGs that characterize crystal structures with a sense of handedness, or structural chirality (Fig. 1a). Spatial inversion, mirror reflection and roto-inversion, that is, a combination of inversion and rotation, all invert structural chirality in crystals³. Of these 230 groups, 65 SGs are free of chirality-inverting symmetries. These chiral SGs correspondingly characterize structurally chiral lattices (Supplementary Section A).

The electronic properties of chiral crystals have been previously recognized as supporting a wide range of phenomena: chiral magnets support skyrmions⁴, chiral metals show non-local and non-reciprocal electron transport^{5,6} and chiral crystals also exhibit optical activity and magnetochiral dichroism⁷. These unusual properties mean it is of great interest to search for possible topological electronic properties in chiral crystals. In this work, we show that structural chirality leads to a universal topological electronic property of all non-magnetic chiral crystals with spin-orbit coupling (SOC), namely, Kramers–Weyl fermions. Although most of the recent theoretical advances in topological semimetals have related band structures to the presence of additional crystalline symmetries (for example, rotation, reflection, non-symmorphic symmetries)^{8–24}, we highlight a class of nodal fermions enforced by structural chirality, and therefore by the absence of particular crystal symmetries.

Tight-binding model of a SOC coupled chiral crystal

Without loss of generality, we present a tight-binding model in the non-symmorphic chiral SG 16 ($P\bar{2}22$) as a representative example. We show that in SG 16, all Kramers degeneracies at time-reversal-invariant

momenta (TRIMs) are Kramers–Weyl nodes with a quantized chiral charge $|C| = 1$. We then use group theory, briefly in this section and exhaustively in Supplementary Section B, to generalize this result and demonstrate that the same arguments apply to all of the TRIMs in non-symmorphic chiral SGs.

SG 16 characterizes a non-centrosymmetric orthorhombic crystal structure with two-fold rotation symmetries along each principle axis, x , y and z . Considering all the symmetry-allowed nearest-neighbour hopping terms, the tight-binding Hamiltonian reads:

$$H(\mathbf{k}) = \sum_{i=x,y,z} t_i^1 \cos(k_i) + t_i^s \sin(k_i) \sigma^i \quad (1)$$

with $t_i^1 \neq t_j^1 \neq t_i^s \neq t_j^s \forall i \neq j$. Here t_i^1 denotes the s -orbital-like hopping strength and t_i^s is a spin-orbit term. By examining the bands at each TRIM at the $\mathbf{k}\cdot\mathbf{p}$ level, we observe that each TRIM hosts a Weyl node described by:

$$H_{\mathbf{k}\cdot\mathbf{p}} = \sum_{i=x,y,z} \left[u_i \left(1 - \frac{k_i^2}{2} \right) + v_i k_i \sigma^i \right] \quad (2)$$

where each TRIM has the same magnitude of u_i and v_i inherited from the lattice hopping parameters, but different TRIM-specific signs. In Fig. 1c,d, we show the band structure for this tight-binding model in the absence and presence of SOC, respectively. The inclusion of SOC splits the spin-degenerate band in Fig. 1c and generates isolated two-fold-degenerate Kramers–Weyl nodes at all of the TRIMs (Fig. 1d)¹⁸. To determine the chiral charge of each Kramers–Weyl node, we examine the direction of the wrapping of

¹Laboratory for Topological Quantum Matter and Advanced Spectroscopy (B7), Department of Physics, Princeton University, Princeton, NJ, USA.

²Centre for Advanced 2D Materials and Graphene Research Centre, National University of Singapore, Singapore, Singapore. ³Department of Physics, National University of Singapore, Singapore, Singapore. ⁴Institute of Physics, Academia Sinica, Taipei, Taiwan. ⁵Department of Physics, Princeton University, Princeton, NJ, USA. ⁶Nordita, Center for Quantum Materials, KTH Royal Institute of Technology and Stockholm University, Stockholm, Sweden. ⁷Department of Physics and Astronomy, University of Pennsylvania, Philadelphia, PA, USA. ⁸Department of Physics, University of Zurich, Zurich, Switzerland. ⁹Department of Physics, National Sun Yat-Sen University, Kaohsiung, Taiwan. ¹⁰Department of Physics, National Cheng Kung University, Tainan, Taiwan. ¹¹Lawrence Berkeley National Laboratory, Berkeley, CA, USA. ¹²These authors contributed equally: Guoqing Chang, Benjamin J. Wieder, Frank Schindler. *e-mail: xusuyang1962@gmail.com; nilnish@gmail.com; mzhasan@princeton.edu

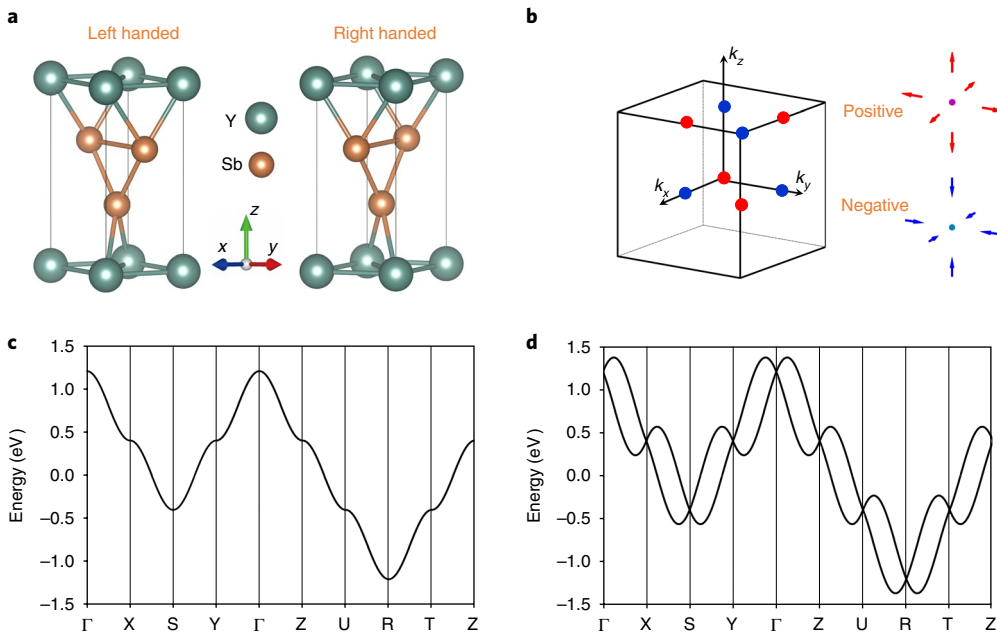


Fig. 1 | Structural chirality, topological chirality and Kramers-Weyl fermions. **a**, Structurally chiral crystals have a distinct handedness, and are therefore characterized by an absence of inversion, mirror or other roto-inversion symmetries³. **b**, Topologically chiral fermions act as monopoles or antimonopoles of Berry curvature. They are characterized by a quantized chiral charge, that is, the quantized Chern number of the occupied bands on a closed surface in momentum space that surrounds the chiral fermion. We found all non-magnetic chiral crystals with SOC host topological chiral fermions at their TRIMs. **c**, The band structure for the SG 16 tight-binding model in the absence of SOC is characterized by a single band with a two-fold spin degeneracy. **d**, The inclusion of SOC splits the bands of this structurally chiral model everywhere except at the TRIMs, where Kramers theorem mandates that the bands remain doubly degenerate. We found that these nodal degeneracies carry the same quantized chiral charge as conventional Weyl fermions, and therefore designate them Kramers-Weyl fermions.

Berry curvature given by the relative signs of the $\{v_i\}$ (the overall sign exchanges the Bloch states of the upper and lower bands) to find the Chern number:

$$C = \prod_{i=x,y,z} \text{sgn}(v_i) \quad (3)$$

This result indicates the chiral charge $C_{+1} = +1 \times \text{sgn}(t_x^s t_y^s t_z^s)$ for the Kramers pairs at TRIM points Γ , S , U and T and $C_{-1} = -1 \times \text{sgn}(t_x^s t_y^s t_z^s)$ for the pairs at X , Y , Z and R , as illustrated in Fig. 1b. The sign of C at Γ reflects the signs of the $\{t_i^s\}$ for the position-space lattice. Thus, the chirality of the atomic positions is directly responsible for defining the handedness of the Kramers-Weyl node at Γ and therefore, by the pattern of alternating signs, at all of the other TRIMs as well.

As our determination of $C = \pm 1$ only relied on the two-fold degeneracy and linear dispersion of equation (2), we deduce that any such degeneracy must be a Weyl node. More precisely, as the little groups of all eight TRIMs in SG 16 are isomorphic to the same chiral point group 222, which with spinful T -symmetry only has a single two-dimensional co-representation^{2,22}, we conclude that any TRIM with a little group isomorphic to point group 222 must also host Kramers-Weyl fermions. Tuning parameters such that $u_i = 0$ and $v_i = v_j$ for all i and j , this $\mathbf{k}\cdot\mathbf{p}$ theory becomes isotropic, and thus invariant under the action of any chiral point group. Taken together, this implies that the little group of the Γ point in an arbitrary chiral crystal, which is isomorphic to the point group of that crystal, and every TRIM point in symmorphic chiral crystals, which host symmetry algebras unmodified by the projections of fractional lattice translations, must always allow at least one irreducible co-representation of a Kramers-Weyl fermion. In Supplementary Section B, we explicitly confirm this conclusion and list the irreducible co-representations

that describe Kramers-Weyl fermions^{2,19,20,23}. We also show in Supplementary Sections C and D that Kramers-Weyl fermions with $|C| = 3$ and non-linear dispersion are permitted in chiral point groups with three- and six-fold rotation symmetries, and in Supplementary Section D we identify the irreducible co-representations of these higher-Chern-number Kramers-Weyl fermions. Previous reports also exploited similar simple models in discussing Weyl fermions^{25,26}. However, they did not explore the relations of the little groups at the TRIMs with each other, and more importantly they did not recognize that their isomorphisms to chiral point groups allow the generalization to other crystal systems.

In non-symmorphic chiral crystals, these arguments become modified away from the Γ point, and the Kramers-Weyl nodes can become obscured by additional band degeneracies. Consider, for example, the chiral SG 19 ($P2_12_12_1$), which differs from SG 16 in that all of its two-fold rotations are, instead, non-symmorphic screws: $s_x = \{C_{2x}|\frac{1}{2} \frac{1}{2} 0\}$, $s_y = \{C_{2y}|\frac{0}{2} \frac{1}{2} \frac{1}{2}\}$ and $s_z = \{C_{2z}|\frac{1}{2} 0 \frac{1}{2}\}$. In reciprocal space, $s_i \times T$ are valid symmetry operations that map a \mathbf{k} point to itself on the $k_i = 0, \pi$ planes. When acting on a Bloch eigenstate of the Hamiltonian, $(s_i T)^2 = e^{-ik_i}$ enforces two-fold Kramers degeneracies throughout all three $k_i = \pi$ planes. TRIMs that belong to exactly two nodal planes will host four-fold degeneracies, due to the algebra of the screw rotations at those \mathbf{k} points. In Supplementary Sections E and F, we examine these nodal surfaces in detail and determine that they exhibit non-zero chiral charges²⁷.

We also note that in certain achiral SGs, it is possible for some of the TRIMs to still have little groups isomorphic to chiral point groups due to the relationship between the SG roto-inversion axes, mirror planes, and the reciprocal lattice vectors. In Supplementary Section G, we explore this possibility and present examples of Kramers-Weyl fermions in achiral crystals.

Table 1 | Representative topological chiral crystals with Kramers–Weyl fermions in symmorphic chiral SGs

SG	Material (code)	Number of collections in the ICSD	SG	Material (code)	Number of collections in the ICSD
1	<i>Li₆CuB₄O₁₀</i> (249215)	492	146	<i>β-Ag₃Si</i> (93431)	307
3	<i>Pb₃GeO₅</i> (200517)	58	149	RbGeO ₆ (73613)	40
5	<i>Ca₂B₅Os₃</i> (59229)	539	150	Tl ₂ TeO ₆ (4321)	314
16	AIPS ₄ (15910)	13	155	<i>Ag₃BO₃</i> (26521)	244
21	YSb ₂ (651733)	51	168	K ₂ Ta ₄ F ₄ O ₉ (8204)	3
22	ThOs ₂ B ₂ (601346)	55	177	PbS ₂ O·4H ₂ O (68630)	3
23	BaAg ₂ SnSe ₄ (170856)	28	195	SnI ₄ (18010)	29
75	K ₄ CuV ₅ ClO ₁₅ (401042)	27	196	<i>α-Cu₂Se</i> (59955)	47
79	AgBi(Cr ₂ O ₇) ₂ (14233)	45	197	m-Bi ₂ O ₃ (27152)	174
89	–	3	207	RbNO ₃ (60966)	1
97	Ta ₂ Se ₈ I (35190)	9	209	Na ₃ PO ₄ (14090)	8
143	RbW ₃ O ₉ (96421)	112	211	NiHg ₄ (151197)	3

We list all 24 symmorphic chiral SGs and, where possible, material candidates from the ICSD³⁰. All the compounds listed in the table host Kramers–Weyl fermions. Among them, the compounds in italic are (semi)metals or small-gap insulators with clean Fermi surfaces and Kramers–Weyl fermions near the Fermi level; their electronic structures are shown in Supplementary Section J. The numbers in brackets are the ICSD collection codes. The SGs in bold may also host additional unconventional four-fold-degenerate chiral fermions at TRIMs with little groups isomorphic to chiral point groups^{9,23,24}, SGs 195, 196 and 197 have TRIM-point little groups isomorphic to chiral point group 23 (*T*)^{23,24}, SGs 207, 209 and 211 have TRIM-point little groups isomorphic to chiral point group 432 (*O*)¹⁹.

Apart from conventional $|C| = 1$ Weyl fermions, all the degeneracies in non-magnetic crystals are captured by the set of irreducible (co)representations²². For each of these degeneracies, a separate calculation of the chiral charge can then be performed. Remarkably, by exhaustively enumerating all of the irreducible (co)representations of the 65 chiral SGs and comparing them to the set of known chiral fermions, now including the Kramers–Weyl fermions highlighted in this work, we find that all the point degeneracies in chiral SGs exhibit a non-zero chiral charge (Supplementary Section N). Specifically, they are either conventional $|C| = 1$ Weyl fermions^{11–13}, double- or triple-Weyl fermions on rotation axes¹⁶, unconventional chiral fermions at high-symmetry crystal momenta^{19,23,24} or Kramers–Weyl fermions. In Supplementary Section O, we compare the symmetry and topology of the Kramers–Weyl fermions with previous examples of conventional and unconventional chiral fermions.

Intrinsic-filling Kramers–Weyl metals also represent the simplest examples of filling-enforced semimetals¹⁸. Although previous works focused on the role of non-symmorphic symmetries in generating large and exotic band connectivities^{18,19,22,23}, we found in this work that even the simplest filling restriction—that is, a *T*-symmetric crystal with an odd number of electrons per unit cell—must be gapless and can be used to predict materials with Weyl fermions. A deeper theoretical understanding of this preference may provide greater insight into the appearance of Mott insulating and other interacting phases in certain filling-enforced semimetals^{28,29}.

Kramers–Weyl physics in known chiral materials

Consulting the Inorganic Crystal Structure Database (ICSD)³⁰, we identify in Tables 1 and 2 representative examples of previously synthesized chiral crystals and highlight in italic the materials in which Kramers–Weyl fermions are relevant to the low-energy physics, which we demonstrate with calculated electronic structures provided in Supplementary Section J. The number of materials varies greatly across the 65 chiral SGs. We found that a large number of known chiral crystals have SGs 4, 19, 173 and 198, whereas SGs 89, 93, 153, 171 and 172 are devoid of promising material candidates.

Among the chiral materials listed in Tables 1 and 2, there are both chiral metals and insulators. Although the Kramers–Weyl nodes in insulators are not generically relevant to transport experiments,

they may still be probed with angle-resolved photoemission spectroscopy^{8,31–33}, scanning tunnelling microscopy⁹, resonant inelastic X-ray scattering³⁴, neutron scattering³⁵ or by optical measurements³⁶. Furthermore, when the Kramers–Weyl nodes of an insulator are near the Fermi level, they could also be studied in transport experiments³⁷ after slight electron or hole doping.

We present two material candidates particularly representative of this physics: a chiral metal and a chiral insulator with spectroscopically accessible Kramers–Weyl Fermi arcs. The band structure of the symmorphic compound *Ag₃BO₃* (no. 26521) (SG 155) is plotted in Fig. 2b,c without and with SOC, respectively; we highlight the Kramers–Weyl nodes with orange circles. As in conventional Weyl semimetals, Kramers–Weyl points also give rise to Fermi arcs which, on surfaces for which bulk TRIMs project onto the surface TRIM points, must necessarily appear in time-reversed pairs. We identified the insulating compound AgBi(Cr₂O₇)₂ (no. 14233) in SG 79 as representative of this physics. The bulk electronic structure of AgBi(Cr₂O₇)₂ in the absence and presence of SOC is shown in Fig. 2f,g, respectively. We confirmed the existence of time-reversed pairs of Fermi arcs at about –0.23 eV below the Fermi energy on the (110) surface (Fig. 2i). A loop taken around one of the surface TRIMs exhibits a projected Chern number of $C = +2$, which necessitates the existence of two Fermi arcs (Fig. 2j). We note that, because the Kramers–Weyl nodes are pinned to the TRIMs, chiral crystals can, in principle, support the longest possible Fermi arcs, and therefore span the entire surface Brillouin zone like those in the unconventional chiral semimetal *β*-RhSi (refs^{23,24}). However, this is very challenging to realize in real materials, for which the bandwidths, determined by the hopping amplitudes, are typically much greater than the spin splitting, which is determined by the strength of the SOC (Supplementary Section I).

Quantum phenomena in chiral crystals

Here we describe five phenomena relevant to the Kramers–Weyl fermions in chiral crystals. Phenomena 1 and 2 are unique to Kramers–Weyl fermions and have not been proposed previously. Phenomena 3–5 were proposed in previous works and are not unique to Kramers–Weyl fermions. Instead, we highlight how Kramers–Weyl fermions provide a previously unrecognized platform for realizing these phenomena.

Table 2 | Representative topological chiral crystals with Kramers–Weyl fermions in non-symmorphic chiral SGs

SG	Material (code)	Number of collections in the ICSD	SG	Material (code)	Number of collections in the ICSD
4	BaCu ₂ Te ₂ O ₆ Cl ₂ (85786)	912	152	IrGe ₄ (53655)	408
17	Ba ₂ Cu ₃ YPb ₂ O ₈ (66088)	29	153	-	1
18	Pd ₇ Se ₄ (77897)	177	154	SrIr ₂ P ₂ (73531)	159
19	α -Ag ₂ Se (261822)	1145	169	α -In ₂ Se ₃ (82203)	55
20	CsCuBr ₃ (10184)	219	170	BaN ₂ O ₄ H ₂ O (201484)	14
24	K ₂ PdSe ₁₀ (71947)	10	171	-	4
76	TIBO ₂ (36404)	64	172	-	1
77	MgB ₂ O(OH) ₆ (24920)	9	173	CuLa ₄ S ₇ (628240)	1238
78	Sr ₂ As ₂ O ₇ (190008)	22	178	Hf ₅ Ir ₃ (638575)	55
80	β -NbO ₂ (35181)	22	179	Na ₃ B ₄ O ₇ Br (252106)	32
90	Na ₂ Ti ₂ Si ₈ O ₂₂ ·4H ₂ O (240912)	20	180	NbGe ₂ (16503)	241
91	Ag ₃ SbO ₄ (417675)	31	181	WAl ₂ (173662)	48
92	MgAs ₄ (1079)	309	182	PbRbIO ₆ (73615)	217
93	-	-	198	β -RhSi (79233)	766
94	H ₆ NaB ₆ ·2H ₂ O (39376)	7	199	K ₂ Sn ₂ O ₃ (40463)	104
95	H ₄ Ca ₂ AsF ₁₃ (415156)	15	208	Zn ₃ As ₂ (24486)	9
96	m-Cu ₂ S (16550)	105	210	H ₆ TeO ₆ (16435)	7
98	CdAs ₂ (16037)	25	212	Li ₂ Pd ₃ B (84931)	152
144	LaBSiO ₅ (39756)	89	213	Mg ₃ Ru ₂ (260022)	221
145	Bi ₂ O ₄ F (172481)	32	214	Ag ₃ Se ₂ Au (171959)	33
151	DyAl ₃ Cl ₁₂ (65975)	48			

We list all 41 non-symmorphic chiral SGs and, where possible, material candidates from the ICSD³⁰. The details are given in Table 1. SGs 198 and 199 have TRIM-point little groups isomorphic to chiral point group 23 (T)^{23,24}, SGs 208, 210, 212, 213 and 214 have TRIM-point little groups isomorphic to chiral point group 432 (O)¹⁹.

Spin texture of Kramers–Weyl fermions. The most general Hamiltonian of a $|C|=1$ Weyl fermion can be written as $H_{\text{Weyl}}(\mathbf{k}) = v_i k_i \sigma_0 + A_{ij} k_j \sigma^i$, where A_{ij} and v_i are real numbers and sums over repeated indices $i,j=x,y,z$ are implied. For the Weyl nodes in a band-inversion Weyl semimetal, σ represents only an effective pseudo-spin degree of freedom, which is very difficult to measure in a momentum-resolved fashion. The physical spin, which can be directly measured by spin-resolved angle-resolved photoemission spectroscopy, is distinct from this pseudo-spin.

Conversely, in the $\mathbf{k}\cdot\mathbf{p}$ theory of Kramers–Weyl fermions, σ represents the true electron spin in the limit in which the energy scale of SOC is much smaller than the interband separation in the absence of SOC (Supplementary Section L). Remarkably, we found that, in this limit, the chiral charge of a Kramers–Weyl fermion can be directly probed by measuring the spin texture. This is a unique property of Kramers–Weyl fermions. Specifically, the physical spin on Fermi surfaces that enclose a Kramers–Weyl node sweeps out the full unit sphere. As the chiral charge is given by $C = \text{sgn}[\det(A)]$, C can be directly obtained by measuring the spin polarization $S_k = \langle \mathbf{k} | \sigma | \mathbf{k} \rangle$ near the Kramers–Weyl nodes by calculating:

$$C^{\text{Kramers–Weyl}} = -\text{sign}(k) \text{sign}(\mathbf{S}_{(k,0,0)} \times \mathbf{S}_{(0,k,0)} \cdot \mathbf{S}_{(0,0,k)}) \quad (4)$$

Moreover, in the presence of additional rotational symmetries, Kramers–Weyl fermions exhibit spin–momentum locking (Supplementary Section L gives a detailed discussion). Specifically, for a $C=+1$ Kramers–Weyl node, the spin either points outward along all three principal directions (for example, k_x , k_y and k_z) or it points outward along one direction and inward along the other two directions; for a $C=-1$ Kramers–Weyl node, the spin either

points inward along all three principal directions, or it points inward along one direction and outward along the other two directions. In addition, T -symmetry enforces $v_i=0$ for Kramers–Weyl fermions, and thus the Kramers–Weyl cone cannot be ‘tilted’ in momentum space³⁸.

Using first-principles calculations, we confirmed the presence of this spin texture in the Kramers–Weyl fermions in Ag₂Se, and contrast it here with that of the conventional band-inversion induced Weyl fermions in TaAs (Fig. 3e,f). In Supplementary Section M, we further show that the real spin–momentum locking of Kramers–Weyl nodes can lead to a large spin Hall conductivity.

Unusually large topologically non-trivial energy windows. A Fermi pocket that encloses a single Weyl node carries a quantized Chern number. Recent reports^{39–41} highlighted that such Fermi pockets can lead to unique transport and symmetry-breaking phenomena, which include magnetic breakdowns³⁹, unconventional quantum oscillations⁴⁰, chiral charge-density waves⁴¹ and giant spin Hall effects⁴².

For a conventional band-inversion-induced Weyl semimetal, isolated chiral Fermi surfaces may only be realized at energies close to the Weyl nodes, which typically are only separated by a few hundredths of the Brillouin zone in momentum, and at less than the order of 100 meV in energy^{31,32}. Therefore, it is quite challenging to realize band-inversion Weyl semimetals with isolated chiral Fermi surfaces; only TaAs and TaP display well-isolated chiral surfaces, whereas in other materials, such as NbP, NbAs and WTe₂, the chemical potential misses the narrow energy window defined by the weak band inversion^{31,32,38}.

In stark contrast, in chiral crystals, isolated Fermi surfaces with a non-vanishing Chern number can form at any energy between

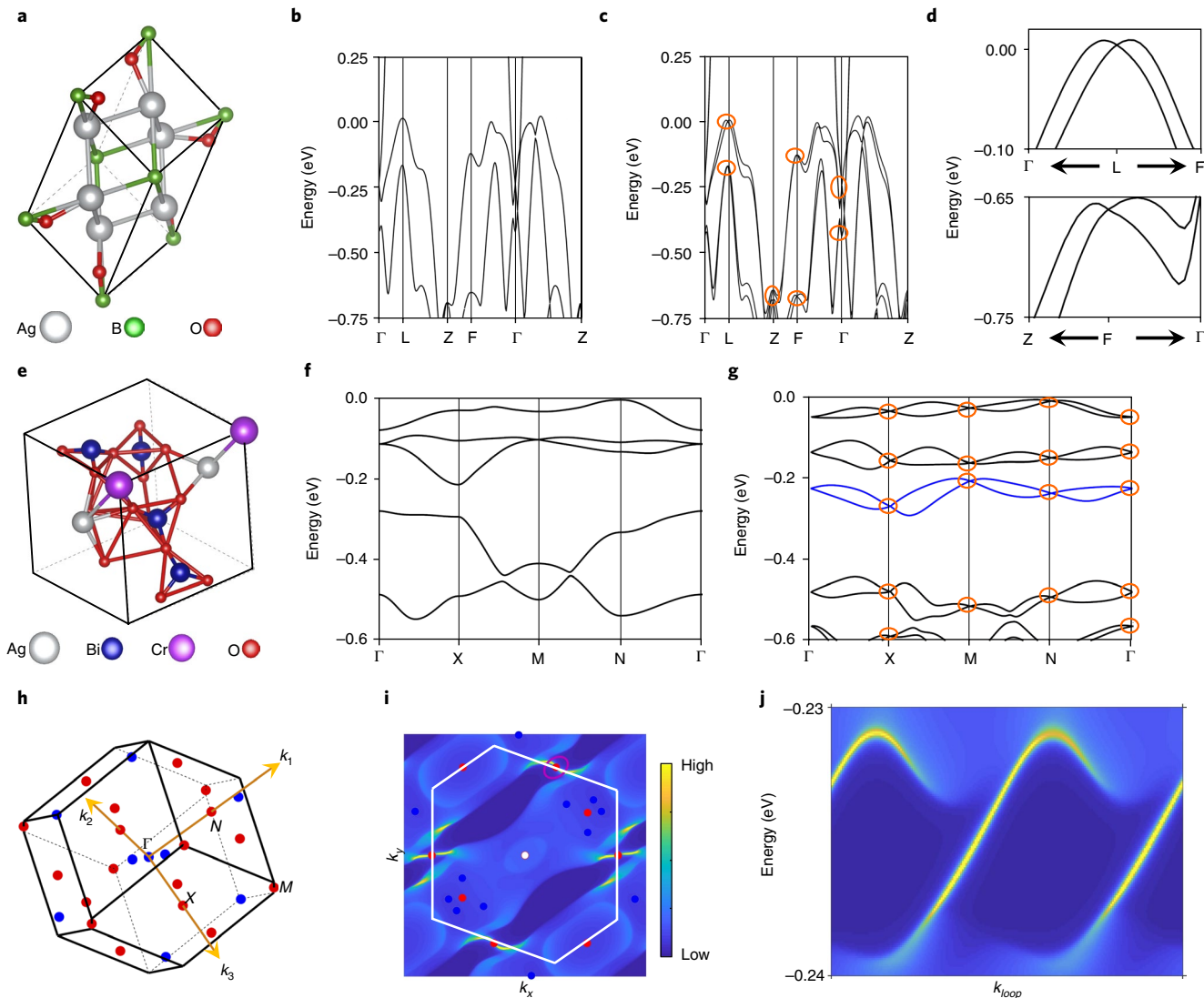


Fig. 2 | Band topology and Fermi arcs of Kramers–Weyl material candidates. **a**, The chiral crystal Ag_3BO_3 in SG 155. **b,c**, The band structures of Ag_3BO_3 passing through TRIMs in the absence (**b**) and presence (**c**) of SOC, respectively. All of the TRIMs in Ag_3BO_3 host isolated Kramers–Weyl nodes in the presence of SOC, as indicated by the orange circles. **d**, The Kramers–Weyl band structures in the vicinity of L (top) and F (bottom). **e–g**, The crystal (**e**), electronic structures of $\text{AgBi}(\text{Cr}_2\text{O}_7)_2$ in SG 79 in the absence (**f**) and presence (**g**) of SOC. **h**, Momentum-space distribution and chiralities of the Weyl nodes in $\text{AgBi}(\text{Cr}_2\text{O}_7)_2$ between the two blue bands in **g**. The red and blue circles indicate Weyl nodes of opposite chiral charges. **i**, The (110) surface state spectral function of $\text{AgBi}(\text{Cr}_2\text{O}_7)_2$ at $E = -0.235$ eV. The Fermi arc surface states that connect the projections of the two distinct bulk pockets are clearly visible. The projected charges of red (blue) circles are +2 (−1). **j**, The surface spectral function along the k path highlighted in **i** exhibits a +2 winding number, consistent with the pair of chiral Fermi arcs observed in **i**.

the highest and the lowest Kramers–Weyl nodes or unconventional chiral fermions in a set of connected bands. The scale of this energy window is governed by the lattice hopping, typically much larger than the accessible scale of band inversion in conventional Weyl semimetals, and the splitting between Fermi surfaces of opposite Chern number is, instead, determined by the strength of the SOC (Fig. 1d and Supplementary Sections H and I).

Quantized circular photogalvanic current. In a recent theoretical work, a quantized circular photogalvanic response effect (CPGE) in roto-inversion-free Weyl semimetals was proposed³⁶, in which Weyl nodes of one chirality sit at the Fermi level and nodes of the opposite chirality lie energetically far away from it. A crucial limitation that has hindered the realization of this phenomena is the lack of viable materials. Indeed, very few Weyl semimetals are known to

satisfy this stringent requirement. In contrast, Kramers–Weyl fermions with opposite chirality are not related by crystal symmetries, and will appear at different energies. Thus, the universal presence of Kramers–Weyl fermions in chiral crystals allows access to a simple, powerful strategy to identify additional ideal material candidates for the observation of quantized photocurrent: identify semimetallic chiral crystals in which a Kramers–Weyl node is isolated at the intrinsic chemical potential, or identify narrow-gap semiconducting chiral crystals in which a Kramers–Weyl node can be isolated by moderate electron or hole doping.

We present $\alpha\text{-Ag}_3\text{Se}_{0.7}\text{Te}_{0.7}$ (SG 19) as an example for doping-enabled photocurrent (Fig. 3). As discussed in Supplementary Section F, crystals in SG 19 display chiral Kramers–Weyl nodes at Γ , and two-fold-degenerate chiral nodal planes along the Brillouin zone boundaries ($k_i = \pi$) (Fig. 3a,b). With slight electron doping,

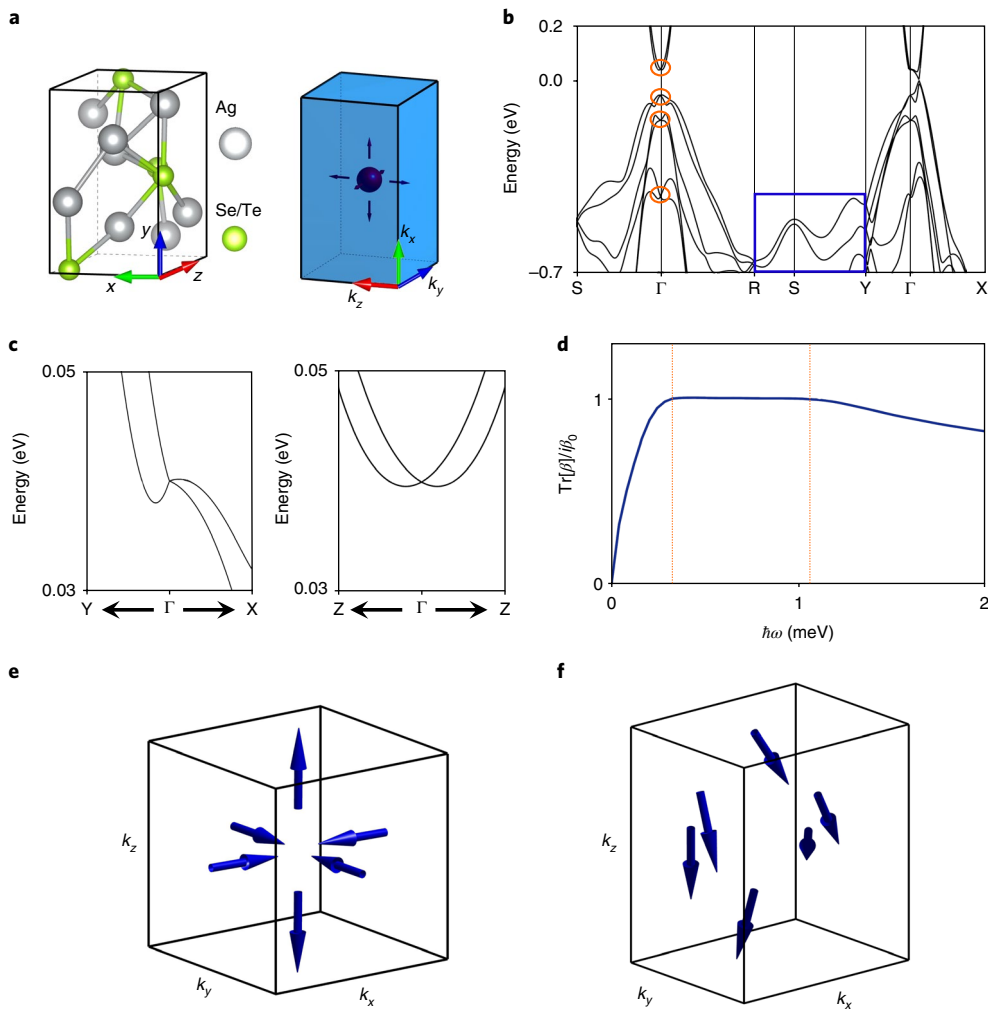


Fig. 3 | Quantized circular photogalvanic current and topological spin-momentum locking. **a**, The chiral crystal $\alpha\text{-Ag}_2\text{Se}_{0.3}\text{Te}_{0.7}$ (left) and the chiral fermions in $\alpha\text{-Ag}_2\text{Se}_{0.3}\text{Te}_{0.7}$ (right) where the Γ point allows an isolated Kramers–Weyl node and the Brillouin zone boundaries feature a nodal surface with a non-zero chiral charge (Supplementary Sections E and F). **b**, The band structure of $\alpha\text{-Ag}_2\text{Se}_{0.3}\text{Te}_{0.7}$ with SOC. The Kramers–Weyl fermions at Γ are highlighted by orange circles. The chiral nodal surfaces are indicated by the blue box. **c**, Bands in the vicinity of the Γ point. **d**, Quantized circular photogalvanic currents induced by the Kramers–Weyl fermions in slightly electron-doped $\alpha\text{-Ag}_2\text{Se}_{0.3-\delta}\text{Te}_{0.7}$ ($\delta=0.16\%$) (whose Fermi level is at the energy of the Kramers–Weyl fermion of conduction bands). β is the multiband gyrotropic photocurrent tensor (Methods) and $\text{Tr}[\beta]$ means the trace of the photocurrent tensor β . $\beta_0=\pi e^3/h^2$ is a quantized constant, where e and h are the electron charge and the Planck constant. $\text{Tr}[\beta]/i\beta_0$ is dimensionless and should reach an integer if the photocurrent is quantized. **e,f**, Real spin along the three principle axes (k_x , k_y , and k_z) for the Kramers–Weyl node near the Fermi level in $\alpha\text{-Ag}_2\text{Se}$ (**e**) and a conventional Weyl node in TaAs (**f**).

one can shift the Fermi level to the Kramers–Weyl fermions. The calculated photogalvanic current of $\alpha\text{-Ag}_2\text{Se}_{0.3-\delta}\text{Te}_{0.7}$ ($\delta=0.16\%$) (Fig. 3d) exhibits a quantized value in the terahertz photon energies (~ 1 meV)⁴³. Continuing with this strategy, we easily identify 16 additional chiral materials for the observation of Kramers–Weyl-enabled quantized photocurrent. These compounds are enumerated along with their band structures in Supplementary Section J.

The chiral magnetic effects. The chiral and gyrotropic effects are linear responses in Weyl semimetals to electromagnetic waves^{44,45}. In these chiral magnetic effects, a dissipationless current arises in response to an alternating magnetic field. These effects are crucially reliant on the same energetic restrictions as the CPGE in the previous section: that Weyl nodes of different chiralities lie at different energies. Like the CPGE, the realization of these effects has been hindered due to the absence of ideal material platforms. Our proposal of Kramers–Weyl fermions immediately provides a feasible platform in which to probe these response effects.

Other exotic phenomena in chiral crystals. Finally, we propose that Kramers–Weyl fermions may offer a way to systematically control and modulate a number of symmetry-allowed phenomena in structurally chiral crystals, including the magnetochiral and magnetoelectric effects^{5,6}. Although these phenomena can still occur in a chiral crystal in the absence of a Weyl node near the Fermi energy, recent theoretical works highlight that the presence of a strong Berry curvature can dramatically enhance the magnitude of these effects⁶. In addition, the presence of Kramers–Weyl fermions near the Fermi energy may offer the possibility to study superconducting pairing on Fermi surfaces with a non-zero Chern number^{46,47}, which may provide a promising recipe for engineering unconventional superconductivity⁴⁸.

Conclusion

In this work, we uncovered a fundamental consequence of the combination of T symmetry and structural chirality in crystals with a spin-orbit interaction. We found that in chiral crystals, the TRIM

points host Kramers–Weyl and other unconventional chiral fermions, or non-symmorphic nodal planes, some of which also exhibit chiral charges^{19,23,24,27} (Supplementary Sections E and F). Kramers–Weyl fermions enable unusual phenomena, such as a monopole-like electron spin texture and topologically non-trivial bulk Fermi surfaces over an unusually large energy window. Given the abundance of previously synthesized chiral crystals, our findings are widely applicable and provide another approach to engineering and controlling the unconventional optical⁷ and transport^{5,6} properties in chiral materials.

Online content

Any methods, additional references, Nature Research reporting summaries, source data, statements of data availability and associated accession codes are available at <https://doi.org/10.1038/s41563-018-0169-3>.

Received: 12 November 2017; Accepted: 15 August 2018;
Published online: 1 October 2018

References

1. Wigner, E. P. On unitary representations of the inhomogeneous Lorentz group. *Ann. Math.* **40**, 149–204 (1939).
2. Bradley, C. J. & Cracknell, A. P. *The Mathematical Theory of Symmetry in Solids* (Clarendon Press Oxford, Oxford, 1972).
3. Flack, H. D. Chiral and achiral crystal structure. *Helv. Chim. Acta* **86**, 905–921 (2003).
4. Bogdanov, A. & Hubert, A. Thermodynamically stable magnetic vortex states in magnetic crystals. *J. Magn. Mater.* **138**, 255–269 (1994).
5. Rikken, G. L. J. A., Fölling, J. & Wyder, P. Electrical magnetochiral anisotropy. *Phys. Rev. Lett.* **87**, 236602 (2001).
6. Yoda, T., Yokoyama, T. & Murakami, S. Current-induced orbital and spin magnetizations in crystals with helical structure. *Sci. Rep.* **5**, 12024 (2015).
7. Fasman, G. D. *Circular Dichroism and the Conformational Analysis of Biomolecules* (Springer, Berlin, 2013).
8. Hasan, M. Z., Xu, S.-Y. & Bian, G. Topological insulators, topological superconductors and Weyl fermion semimetals. *Phys. Scr.* **T164**, 014001 (2015).
9. Zheng, H. & Hasan, M. Z. Quasiparticle interference on type-I and type-II Weyl semimetal surfaces: a review. *Adv. Phys. X* **3**, 146661 (2018).
10. Yang, B. J. & Nagaosa, N. Classification of stable three-dimensional Dirac semimetals with nontrivial topology. *Nat. Commun.* **5**, 4898 (2015).
11. Murakami, S. Phase transition between the quantum spin Hall and insulator phases in 3D: emergence of a topological gapless phase. *New J. Phys.* **9**, 356 (2007).
12. Wan, X. et al. Topological semimetal and Fermi-arc surface states in the electronic structure of pyrochlore iridates. *Phys. Rev. B* **83**, 205101 (2011).
13. Burkov, A. A. & Balents, L. Weyl semimetal in a topological insulator multilayer. *Phys. Rev. Lett.* **107**, 127205 (2011).
14. Young, S. M. et al. Dirac semimetal in three dimensions. *Phys. Rev. Lett.* **108**, 140405 (2012).
15. Mañes, J. L. Existence of bulk chiral fermions and crystal symmetry. *Phys. Rev. B* **85**, 155118 (2012).
16. Fang, C. et al. Multi-Weyl topological semimetals stabilized by point group symmetry. *Phys. Rev. Lett.* **107**, 127205 (2011).
17. Kim, W., Wieder, B. J., Kane, C. L. & Rappe, A. M. Dirac line nodes in inversion-symmetric crystals. *Phys. Rev. Lett.* **115**, 036806 (2015).
18. Watanabe, H. et al. Filling constraints for spin-orbit coupled insulators in symmorphic and nonsymmorphic crystals. *Proc. Natl Acad. Sci. USA* **112**, 14551–14556 (2015).
19. Bradlyn, B. et al. Beyond Dirac and Weyl fermions: unconventional quasiparticles in conventional crystal. *Science* **353**, aaf5037 (2016).
20. Wieder, B. J. et al. Double Dirac semimetals in three dimensions. *Phys. Rev. Lett.* **116**, 186402 (2016).
21. Po, H. C., Vishwanath, A. & Watanabe, H. Topological materials discovery using electron filling constraints. *Nat. Phys.* **14**, 55–61 (2018).
22. Bradlyn, B. et al. Topological quantum chemistry. *Nature* **547**, 298–305 (2017).
23. Chang, G. et al. Unconventional chiral fermions and large topological Fermi arcs in RhSi. *Phys. Rev. Lett.* **119**, 206401 (2017).
24. Tang, P., Zhou, Q. & Zhang, S.-C. Multiple types of topological fermions in transition metal silicides. *Phys. Rev. Lett.* **119**, 206402 (2017).
25. Witczak-Krempa, W., Knap, M. & Abanin, D. Interacting Weyl semimetals: characterization via the topological Hamiltonian and its breakdown. *Phys. Rev. Lett.* **113**, 136402 (2014).
26. Bernevig, B. A. *Lecture on Weyl semimetals at the Topological Matter School*, Donostia International Physics Center (Topological Matter School, 2016); <https://tms16.sciencesconf.org/>; <https://www.youtube.com/watch?v=j0zgWHLL1z4>
27. Xiao, M. & Fan, S. Topologically charged nodal surface. Preprint at <https://arxiv.org/abs/1709.02363> (2017).
28. Sharma, G. et al. Electronic structure, photovoltaic, and photocatalytic hydrogen evolution with p-CuBi₂O₄ nanocrystals. *J. Mater. Chem. A* **4**, 2936–2942 (2016).
29. Di Sante, D. et al. Realizing double Dirac particles in the presence of electronic interactions. *Phys. Rev. B* **96**, 121106(R) (2017).
30. Inorganic Crystal Structure Database (FIZ Karlsruhe, 2014); <http://icsd.fiz-karlsruhe.de/icsd>
31. Xu, S.-Y. et al. Discovery of a Weyl fermion semimetal and topological Fermi arcs. *Science* **349**, 613–617 (2015).
32. Lv, B. Q. et al. Experimental discovery of Weyl semimetal TaAs. *Phys. Rev. X* **5**, 031013 (2015).
33. Lu, L. et al. Experimental observation of Weyl points. *Science* **349**, 622–624 (2015).
34. Kourtis, S. Bulk spectroscopic measurement of the topological charge of Weyl nodes with resonant x-rays. *Phys. Rev. B* **94**, 125132 (2016).
35. Itoh, S. Weyl Fermions and spin dynamics of metallic ferromagnet SrRuO₃. *Nat. Commun.* **7**, 11788 (2016).
36. de Juan, F. et al. Quantized circular photogalvanic effect in Weyl semimetals. *Nat. Commun.* **8**, 15995 (2017).
37. Xiong, J. et al. Evidence for the chiral anomaly in the Dirac semimetal Na₃Bi. *Science* **350**, 413–416 (2014).
38. Soluyanov, A. A. et al. Type-II Weyl semimetals. *Nature* **527**, 495–498 (2015).
39. Chan, C.-K. & Lee, P. A. Emergence of bulk gap and metallic side walls in the zeroth Landau level in Dirac and Weyl semimetals. *Phys. Rev. B* **96**, 195143 (2017).
40. Hu, J. et al. π Berry phase and Zeeman splitting of TaP probed by high field magnetotransport measurements. *Sci. Rep.* **6**, 18674 (2016).
41. Wang, Z. & Zhang, S.-C. Chiral anomaly, charge density waves, and axion strings from Weyl semimetals. *Phys. Rev. B* **87**, 161107(R) (2013).
42. Sun, Y., Zhang, Y., Felser, C. & Yan, B. Giant intrinsic spin Hall effect in the TaAs family of Weyl semimetals. *Phys. Rev. Lett.* **117**, 146403 (2016).
43. Shan, J. & Heinz, T. F. *Ultrafast Dynamical Processes in Semiconductors* (Springer, Berlin, 2004).
44. Zyuzin, A. A. et al. Weyl semimetal with broken time reversal and inversion symmetries. *Phys. Rev. B* **85**, 165110 (2012).
45. Zhong, S., Moore, J. E. & Souza, I. Gyrotropic magnetic effect and the magnetic moment on the Fermi surface. *Phys. Rev. Lett.* **116**, 077201 (2016).
46. Bardarson, J. H., Lu, Y.-M. & Moore, J. E. Superconductivity of doped Weyl semimetals: finite-momentum pairing and electronic analogues of the ³He-A phase. *Phys. Rev. B* **86**, 214514 (2012).
47. Hosur, P. & Qi, X.-L. Time-reversal invariant topological superconductivity in doped Weyl semimetals. *Phys. Rev. B* **90**, 045130 (2014).
48. Xu, S.-Y. et al. Momentum-space imaging of Cooper pairing in a half-Dirac-gas topological superconductor. *Nat. Phys.* **10**, 943–950 (2014).

Acknowledgements

Work at Princeton was supported by the US Department of Energy under Basic Energy Sciences (grant no. DOE/BES DE-FG-02-05ER46200). M.Z.H. acknowledges Visiting Scientist support from the Lawrence Berkeley National Laboratory, and partial support for theoretical work from the Gordon and Betty Moore Foundation (grant no. GBMF4547/Hasan). The work at the National University of Singapore was supported by the National Research Foundation, Prime Minister's Office, Singapore, under its NRF fellowship (NRF award no. NRF-NRFF2013-03). B.J.W. acknowledges support through a Simons Investigator grant from the Simons Foundation to C. L. Kane, through Nordita under ERC DM 321031, through grants from the Department of Energy (no. DE-SC0016239), the Simons Foundation (Simons Investigator grant no. ONR-N00014-14-1-0330), the Packard Foundation and the Schmidt Fund to B. A. Bernevig, and acknowledges the hospitality of the Donostia International Physics Center. F.S. and T.N. acknowledge support by the Swiss National Science Foundation (grant no. 200021-169061) and the ERC-StG-Neupert-757867-PARATOP, respectively. T.-R.C. was supported by the Ministry of Science and Technology under the MOST Young Scholar Fellowship: MOST Grant for the Columbus Program no. 107-2636-M-006-004-, National Cheng Kung University, Taiwan, and the National Center for Theoretical Sciences (NTCTS), Taiwan. M.Z.H. acknowledges support from the Miller Institute of Basic Research in Science at the University of California at Berkeley in the form of a Visiting Miller Professorship during the early stages of this work. The authors thank C. L. Kane and R. Kamien for helpful discussions on chirality and thank B. Bradlyn, J. Cano, M. I. Aroyo and B. A. Bernevig for insightful discussions on group theory and symmetry.

Author contributions

All the authors contributed to the intellectual content of this work. By systematically studying the electronic structures of chiral crystals, the existence of Weyl points at TRIM

points of chiral crystals was recognized by G.C. and S.-Y.X. in consultation with M.Z.H. B.J.W. proved that Weyl fermions at TRIM points (Kramers–Weyl fermions) are a generic feature of all chiral crystals, and thus that all point degeneracies in chiral crystals are topological. F.S. and T.N. proved the relationship between bulk symmetry eigenvalues and the chiral charge of Kramers–Weyl fermions. Spin–momentum locking was proposed by F.S. and T.N., and applied to models and materials by B.J.W., S.-Y.X and G.C. The materials search was done by G.C. and S.-Y.X. with help from all the authors. Tight-binding models were constructed by B.J.W., F.S. and T.N. The first-principles calculations were performed by G.C., S.-M.H., B.S., D.W., T.-R.C. and H.L. The manuscript was written by G.C., B.J.W., F.S., T.N., S.-Y.X., H.L. and M.Z.H. with the help of D.S.S. and I.B. S.-Y.X., H.L. and M.Z.H. were responsible for the overall research direction, planning and integration among different research units.

Competing interests

The authors declare no competing interests.

Additional information

Supplementary information is available for this paper at <https://doi.org/10.1038/s41563-018-0169-3>.

Reprints and permissions information is available at www.nature.com/reprints.

Correspondence and requests for materials should be addressed to S.-Y.X. or H.L. or M.Z.H.

Publisher's note: Springer Nature remains neutral with regard to jurisdictional claims in published maps and institutional affiliations.

Methods

We performed first-principles calculations within the density functional theory framework using the projector augmented wave method as implemented in the VASP⁴⁹ package and the full-potential augmented plane-wave method as implemented in the package Wien2k⁵⁰. The generalized gradient approximation was used⁵¹. The lattice constants for the materials examined in this paper were obtained from the ICSD³⁶. To calculate the surface states of AgBi(Cr_xO₇)₂, Wannier functions were generated using the *d* orbitals of Ag, the *p* and *d* orbitals of Cr and the *p* orbitals of O. The surface states were calculated for a semi-infinite slab by the iterative Green's function method.

To calculate the circular photogalvanic current in $\alpha\text{-Ag}_2\text{Se}_{0.3}\text{Te}_{0.7}$ (SG 19), we generated the Wannier functions of $\alpha\text{-Ag}_2\text{Se}$ (SG 19) and $\alpha\text{-Ag}_2\text{Te}$ (SG 19) using the *s* and *d* orbitals of Ag and the *p* orbitals of Se and Te. The electronic structure of $\alpha\text{-Ag}_2\text{Se}_{0.3}\text{Te}_{0.7}$ (SG 19) was calculated by a linear interpolation between tight-binding model matrix elements of $\alpha\text{-Ag}_2\text{Se}$ (SG 19) and $\alpha\text{-Ag}_2\text{Te}$ (SG 19). We calculated the multiband gyrotropic photocurrent tensor $\beta_{ij}(\omega)$ (ref. ³⁶) to obtain the circular photogalvanic effect photocurrent rate:

$$\beta_{ij}(\omega) = \frac{i\pi e^3}{\hbar} \epsilon_{jkl} \sum_{\mathbf{k}, n, m} f_{nm}^{\mathbf{k}} \Delta_{\mathbf{k}, nm}^i r_{\mathbf{k}, nm}^{\mathbf{k}} r_{\mathbf{k}, mn}^l \delta(\hbar\omega - E_{\mathbf{k}, mn}) \quad (5)$$

Data availability

The data supporting the findings of this study are available within the paper and other findings of this study are available from the corresponding author upon reasonable request.

References

49. Kresse, G. & Furthmöller, J. Efficiency of ab-initio total energy calculations for metals and semiconductors using a plane-wave basis set. *Comput. Mater. Sci.* **6**, 15–50 (1996).
50. Blaha, P., Schwarz, K. & Madsen, G. K. H. et al. *An Augmented Plane Wave plus Local Orbital Program for Calculating Crystal Properties*. (Vienna University of Technology, Vienna, 2001).
51. Perdew, J. P., Burke, K. & Ernzerhof, M. Generalized gradient approximation made simple. *Phys. Rev. Lett.* **77**, 3865 (1996).

In the format provided by the authors and unedited.

Topological quantum properties of chiral crystals

Guoqing Chang ^{1,2,3,4,12}, Benjamin J. Wieder ^{5,6,7,12}, Frank Schindler^{8,12}, Daniel S. Sanchez¹, Ilya Belopolski¹, Shin-Ming Huang ⁹, Bahadur Singh ^{2,3}, Di Wu^{2,3}, Tay-Rong Chang¹⁰, Titus Neupert ⁸, Su-Yang Xu^{1*}, Hsin Lin^{2,3,4*} and M. Zahid Hasan ^{1,11*}

¹Laboratory for Topological Quantum Matter and Advanced Spectroscopy (B7), Department of Physics, Princeton University, Princeton, NJ, USA.

²Centre for Advanced 2D Materials and Graphene Research Centre, National University of Singapore, Singapore, Singapore. ³Department of Physics,

National University of Singapore, Singapore, Singapore. ⁴Institute of Physics, Academia Sinica, Taipei, Taiwan. ⁵Department of Physics, Princeton University, Princeton, NJ, USA. ⁶Nordita, Center for Quantum Materials, KTH Royal Institute of Technology and Stockholm University, Stockholm, Sweden. ⁷Department of Physics and Astronomy, University of Pennsylvania, Philadelphia, PA, USA. ⁸Department of Physics, University of Zurich, Zurich, Switzerland. ⁹Department of Physics, National Sun Yat-Sen University, Kaohsiung, Taiwan. ¹⁰Department of Physics, National Cheng Kung University, Tainan, Taiwan. ¹¹Lawrence Berkeley National Laboratory, Berkeley, CA, USA. ¹²These authors contributed equally: Guoqing Chang, Benjamin J. Wieder, Frank Schindler. *e-mail: xusuyang1962@gmail.com; nilnish@gmail.com; mzhasan@princeton.edu

This file includes:

- SI A. Other Notions of Chirality in Group Theory
- SI B. Group Theory for Kramers-Weyl Fermions
- SI C. Allowed Degeneracies in the Presence of \mathcal{C}_n Rotation Symmetries
- SI D. Kramers-Weyl Nodes have an Odd Chern Number
- SI E. Nodal Degeneracies in Nonsymmorphic Chiral Space Groups
- SI F. Topology of Nodal Surfaces in Nonsymmorphic Chiral Space Groups
- SI G. Kramers-Weyl Nodes in Achiral Space Groups
- SI H. Fermi Surface Analysis of Kramers-Weyl Materials
- SI I. Fermi Arcs in Kramers-Weyl Metals
- SI J. Additional Kramers-Weyl Materials
- SI K. Weyl Nodes Distribution in $\text{AgBi}(\text{Cr}_2\text{O}_7)_2$
- SI L. Theory for Novel Spin Texture of Kramers-Weyl Fermions
- SI M. Calculated Spin Texture near Kramers-Weyl Points
- SI N. Nonzero Chern Numbers of all Point Degeneracies in Chiral Crystals
- SI O. Comparison of Kramers-Weyl Fermions and Other Chiral Fermions

SI A. Other Notions of Chirality in Group Theory

In this work, we refer to a space group (SG) as chiral if it characterizes an “enantiomeric” crystal, or one with no reflection planes or roto-inversion centers. There is also a separate, mathematical concept of chiral space group that is distinct from the definition employed in this work; in those systems, it is the group algebra itself which possesses a notion of handedness. These 22 *algebraically* chiral groups, also known as the “enantiomorphic” groups, comprise the subset of the 65 chiral, or Sohncke, SGs, for which the operation of inversion changes not only the structural handedness of the crystal lattice, but also the set of symmetry operations in the SG [1].

SI B. Group Theory for Kramers-Weyl Fermions

Here, we provide a more formal definition of a Kramers-Weyl node in the language of group theory and irreducible representations. Kramers-Weyl fermions are defined as two-dimensional, double-valued irreducible corepresentations of little groups that are isomorphic to the time-reversal-symmetric chiral point groups. The chiral, or enantiomorphic, point groups are defined as those lacking rotoinversions [2, 3], and are therefore given by a short list: 1, 2, 3, 4, 6, 222, 422, 622, 32, 23, and 432.

It has been shown in previous works [4, 5] that bands in strong-spin-orbit systems must be singly-degenerate when dispersing from Γ in crystals with 3D symmetries, and therefore the two-dimensional irreducible corepresentations presented here will always have well-defined Chern numbers. In the cases of nonsymmorphic groups, the little groups at the zone-edge TRIMs can contain projective representations modified by fractional lattice translations, and will therefore no longer be isomorphic to those at Γ . They thus will no longer be generically isomorphic to point groups. However, we can state that in symmorphic chiral crystals, the little groups at all of the TRIMs will be isomorphic to time-reversal-symmetric chiral point groups, and thus will be able to host Kramers-Weyls fermions (though we note that in body- and face-centered crystals, some of the TRIMs may be isomorphic to different chiral point groups).

We can use Bradley and Cracknell [1] to list the abstract groups and irreducible corepresentations that describe Kramers-Weyl fermions. They are listed in Table S1, obtained

by considering the allowed irreducible corepresentations at Γ for crystals in space groups which modulo translations are isomorphic to the chiral point groups. We list a point group under two different naming conventions, give the simplest space group that generates crystals in this point group, and list the abstract groups and irreducible corepresentations of the Kramers-Weyl node for each of the chiral point groups.

We can also use the results of SI C and Ref. [6] to determine the magnitudes of the Chern numbers $|C|$ of the Kramers-Weyl points described by the corepresentations listed in Table S1. Kramers-Weyl fermions with Chern numbers $|C| = 3$ must have C_3 eigenvalues of -1 , or C_6 eigenvalues of $\pm i$; all other chiral two-fold degeneracies with well-defined rotation eigenvalues must have Chern numbers $|C| = 1$. Therefore, considering the action of time-reversal symmetry on the eigenvalues, we search for corepresentations with either:

$$\chi_{\tilde{\rho}}(C_3) = -2 \text{ or } \chi_{\tilde{\rho}}(C_6) = 0, \quad (\text{S1})$$

where $\chi_{\tilde{\rho}}(g)$ is the character of the point group element g for the corepresentation $\tilde{\rho}$.

Irreducible Corepresentations of Kramers-Weyl Fermions				
Point Group Name 1	Point Group Name 2	Simplest SG	Abstract Group and Corepresentations under \mathcal{T}	Magnitude of Chern Number ($ C $)
1	C_1	1	$G_2^1 : R_2R_2$	1
2	C_2	3	$G_4^1 : R_2R_4$	1
222	D_2	16	$G_8^5 : R_5$	1
4	C_4	75	$G_8^1 : R_2R_8, R_4R_6$	1
422	D_4	89	$G_{16}^{14} : R_6, R_7$	1
3	C_3	143	$G_6^1 : R_2R_6$	1
			$G_6^1 : R_4R_4$	3
32	D_3	149	$G_{12}^4 : R_3R_4$	3
			$G_{12}^4 : R_6$	1
6	C_6	168	$G_{12}^1 : R_2R_{12}, R_6R_8$	1
			$G_{12}^1 : R_4R_{10}$	3
622	D_6	177	$G_{24}^{11} : R_7$	3
			$G_{24}^{11} : R_8, R_9$	1
23	T	195	$G_{24}^9 : R_4$	1
432	O	207	$G_{48}^{10} : R_4, R_5$	1

TABLE S1: The irreducible corepresentations of Kramers-Weyl fermions as labeled in Ref. [1].

SI C. Allowed Degeneracies in the Presence of \mathcal{C}_n Rotation Symmetries

In this section we study whether rotational symmetry \mathcal{C}_n , $n = 2, 3, 4, 6$ can enforce Kramers-Weyl nodes with chiral charge $|C| > 1$. In the absence of time-reversal symmetry, generic Weyl nodes located on a \mathcal{C}_n rotation axis were studied in Ref. [7]. It was found that \mathcal{C}_n with $n = 2, 3$ can only protect Weyl nodes with $C = \pm 1$, \mathcal{C}_4 symmetry can protect Weyl nodes with both $C = \pm 1$ and $C = \pm 2$, and \mathcal{C}_6 symmetry can protect Weyl nodes with $C = \pm 1$, $C = \pm 2$, and $C = \pm 3$. According to these findings, we in this section analyze cases with all values of n to determine which are compatible with time-reversal symmetry and, therefore, are allowed at a Kramers-Weyl node.

To determine the possible kinds of degeneracies, we make use of the general classification scheme developed in Ref. [7]: we first note that for a spinless case, the eigenvalues of \mathcal{C}_n in the filled subspace are taken out of the set of the n -th roots of $+1$. In addition, time-reversal symmetry forces them to either be real or to come in complex-conjugated pairs. The same holds for the case of spinful bands, where the eigenvalues are further split and taken out of the set of the n -th roots of -1 . Furthermore, taking every spinless eigenvalue χ of \mathcal{C}_n belonging to a certain band that splits when introducing spin, we can uniquely assign two spinful eigenvalues for the split bands, which are determined by $u = \chi e^{\pm i\pi/n}$. The nature of the crossing between spinful bands is now determined by the fraction u_c/u_v , where u_c and u_v are the time-reversal paired eigenvalues. From this fraction, the absolute value of the chiral charge $|C|$ can be read off from Tab. I in Ref. [7], see Tab. S2 and S3.

From the content of this table, we can conclude that time-reversal symmetry in combination with \mathcal{C}_4 symmetry allows only for $C = \pm 1$ Weyl nodes, while its combination with \mathcal{C}_6 symmetry is additionally compatible with $C = \pm 3$ Weyl nodes. In the latter case, a spinless Kramers-Weyl node $C = \pm 1$ at the Kramers point is split by spin-orbit coupling into two Weyl nodes, one with $C = \pm 1$, and another with $C = \pm 3$. An analysis of the irreducible representations in chiral space groups with \mathcal{C}_6 symmetry, such as in the simple example of SG 168 *P6*, confirms the allowed presence of both $C = |1|$ and $C = |3|$ Kramers-Weyl nodes [1]. Note that as pointed out by Tsirkin *et al.* in Ref. [6], in the case of \mathcal{C}_3 symmetry there is one additional possibility, which is not captured by restricting the classification of Ref. [7] to time-reversal-symmetric systems: when a Kramers pair of bands has a real spinful \mathcal{C}_3 eigenvalue, it may only cross in a Weyl node with chiral charge $C = \pm 3$.

\mathcal{C}_4	spinless eigenvalues	spinful eigenvalues	u_c/u_v	$ C $
	+1	$\{e^{i\frac{\pi}{4}}, e^{-i\frac{\pi}{4}}\}$	$\pm i$	1
	-1	$\{-e^{i\frac{\pi}{4}}, -e^{-i\frac{\pi}{4}}\}$	$\pm i$	1
	$\{+i, -i\}$	$(\{e^{i\frac{3\pi}{4}}, e^{-i\frac{3\pi}{4}}\}, \{e^{i\frac{\pi}{4}}, e^{-i\frac{\pi}{4}}\})$	$(\pm i, \pm i)$	(1, 1)

TABLE S2: Properties of allowed \mathcal{C}_4 band crossings at Kramers points. The first two lines each correspond to a single, spin-degenerate band, which splits under spin-orbit coupling into two bands that cross at a Kramers-Weyl node with unit chiral charge. The last line describes the splitting of two spin-degenerate bands, forming a spinless Weyl cone at a TRIM into four bands, which exhibit two Kramers crossings of unit chiral charge, respectively.

\mathcal{C}_6	spinless eigenvalues	spinful eigenvalues	u_c/u_v	$ C $
	+1	$\{e^{i\frac{\pi}{6}}, e^{-i\frac{\pi}{6}}\}$	$e^{\pm i\frac{\pi}{3}}$	1
	-1	$\{-e^{i\frac{\pi}{6}}, -e^{-i\frac{\pi}{6}}\}$	$e^{\pm i\frac{\pi}{3}}$	1
	$\{e^{i\frac{\pi}{3}}, e^{-i\frac{\pi}{3}}\}$	$(\{e^{i\frac{3\pi}{6}}, e^{-i\frac{3\pi}{6}}\}, \{e^{i\frac{\pi}{6}}, e^{-i\frac{\pi}{6}}\})$	$(-1, e^{\pm i\frac{\pi}{3}})$	(3, 1)
	$\{e^{i\frac{2\pi}{3}}, e^{-i\frac{2\pi}{3}}\}$	$(\{e^{i\frac{5\pi}{6}}, e^{-i\frac{5\pi}{6}}\}, \{e^{i\frac{3\pi}{6}}, e^{-i\frac{3\pi}{6}}\})$	$(e^{\pm i\frac{\pi}{3}}, -1)$	(1, 3)

TABLE S3: Properties of allowed \mathcal{C}_6 band crossings at Kramers points. The first two lines each correspond to a single, spin-degenerate band, which splits under spin-orbit coupling into two bands that cross at a Kramers-Weyl nodes with unit chiral charge. The third and fourth lines both describe the splitting of two spin-degenerate bands crossing at a TRIM into four bands, which exhibit two different Kramers crossings: one of unit chiral charge and another of chiral charge 3.

SI D. Kramers-Weyl Nodes have an Odd Chern Number

In this section we show that for a time-reversal-invariant two-band Hamiltonian $H(\mathbf{k}) = \mathbf{d}(\mathbf{k}) \cdot \hat{\boldsymbol{\sigma}}$ with $\mathcal{T}^2 = -1$, the Chern number of a (Fermi) surface enclosing a TRIM is always odd. Here, the elements of vector $\hat{\boldsymbol{\sigma}}$ are the three Pauli matrices and \mathbf{k} lives in three-dimensional momentum space. Time-reversal symmetry can be represented by $\mathcal{T} = Ki\sigma^y$, which flips the spin $\mathcal{T}\hat{\boldsymbol{\sigma}}\mathcal{T}^{-1} = -\hat{\boldsymbol{\sigma}}$. Therefore, time-reversal symmetry of the Hamiltonian $\mathcal{T}H(\mathbf{k})\mathcal{T}^{-1} = H(-\mathbf{k})$ implies $\mathbf{d}(\mathbf{k}) = -\mathbf{d}(-\mathbf{k})$.

Since the Chern number of a surface in momentum space is a topological quantity, we may choose our manifold of integration to be the unit sphere S_0^2 centered at the origin (the TRIM) without loss of generality. The Chern number is then given by

$$C = \frac{1}{2\pi} \int_{S_0^2} dA, \quad A = i \langle u(\mathbf{k}) | d | u(\mathbf{k}) \rangle, \quad (\text{S2})$$

where d is the exterior derivative and $|u(\mathbf{k})\rangle$ denotes the eigenvector of $H(\mathbf{k})$ belonging to its lower eigenvalue. Note that since the Hamiltonian is gapped on S_0^2 , we can take $|\mathbf{d}(\mathbf{k} \in S_0^2)| = 1$ without loss of generality.

Due to the antisymmetry of $\mathbf{d}(\mathbf{k})$ on this sphere, there will always be a singly-connected time-reversal-invariant closed loop $\mathcal{C}_{dz=0} \subset S_0^2$ of \mathbf{k} -points on which $d^z(\mathbf{k}) = 0$. On the loop $\mathcal{C}_{dz=0}$, we may then re-express the Hamiltonian as

$$H(\mathbf{k}) = \begin{pmatrix} 0 & e^{-i\Phi(\mathbf{k})} \\ e^{i\Phi(\mathbf{k})} & 0 \end{pmatrix}, \quad \Phi(\mathbf{k}) = \Phi(-\mathbf{k}) + (2k+1)\pi, \text{ where } k \in \mathbb{Z}, \quad (\text{S3})$$

where the second equality follows from time-reversal symmetry. It is now straightforward to solve for $A = \frac{1}{2}\partial_\phi\Phi(\phi)$, where $\phi \in [0, 2\pi]$ denotes an angle parametrizing $\mathcal{C}_{dz=0}$. For parallel transport around any closed loop on the Bloch sphere, we have the relation

$$\exp\left(i \oint_{\mathcal{C}} A\right) = \exp\left(i \int_{\Lambda} dA\right), \quad (\text{S4})$$

where Λ is a two-dimensional submanifold of the sphere and \mathcal{C} is its boundary.

Since by time-reversal symmetry, the segments of the sphere separated by $\mathcal{C}_{dz=0}$ yield the same contribution to the Chern number, we can use Eq. (S4) to arrive at

$$C = 2 \left(\frac{1}{2\pi} \oint_{\mathcal{C}_{dz=0}} A + m \right) = \frac{1}{2\pi} \int_0^{2\pi} d\phi \partial_\phi \Phi(\phi) + 2m, \quad m \in \mathbb{Z}. \quad (\text{S5})$$

Note that the periodicity of $\Phi(\phi)$ implies $\Phi(2\pi) = \Phi(0) + 2\pi n$, where $n \in \mathbb{Z}$. Together with the constraint imposed by time-reversal symmetry above, we actually even gain the stronger constraint $\Phi(2\pi) = \Phi(0) + 2\pi(2k + 1)$, where $k \in \mathbb{Z}$, i.e., n is an odd integer. This implies that $C = 2(k + m) + 1$ is odd and, therefore, that Kramers-Weyl nodes have an odd Chern number.

SI E. Nodal Degeneracies in Nonsymmorphic Chiral Space Groups

In this section we discuss the effects of nonsymmorphic symmetries in chiral space groups on the band structures near TRIM points at the BZ boundary. For a subset of nonsymmorphic chiral space groups, all Kramers degeneracies at the TRIMs will have \mathcal{T} -pinned Kramers-Weyl nodes. However, another subset will have Kramers degeneracies that form nodal planes, instead of isolated Weyl nodes due to the relationship between their screw rotation axes and time-reversal-symmetry.

The zone-boundary degeneracy structure in nonsymmorphic chiral crystals is strongly affected by the presence of nodal planes, which can form when certain screw rotation symmetries combine with time-reversal symmetry. For a crystal symmetry Π to combine with time-reversal to protect a two-fold degeneracy away from a TRIM, $\mathcal{T} \times \Pi$ must return \mathbf{k} to itself and square to -1 for that value of \mathbf{k} . Thus, in a \mathcal{T} -symmetric crystal with this Π symmetry, bands will be at least two-fold degenerate at $\mathcal{T} \times \Pi$ -invariant \mathbf{k} -points in the Brillouin zone (BZ). The modified algebra of the screw rotations at $k_i = \pi$ can also be understood by noting that the little groups of those TRIMs are no longer isomorphic to those at Γ , as they were in SG 16, due to the projective effects of the fractional lattice translations on the commutation relations of the symmetry representations [8]. To illustrate this more clearly, we use Te and IrSn₄ as real crystal examples (Figs. S1a-c). The crystal lattice of Te is represented by the nonsymmorphic chiral space group 4 (SG 4) and, as a result, has a $s_z = \{\mathcal{C}_{2z}|00\frac{1}{2}\}$ screw-rotation symmetry. Therefore, for the case of Te, \mathcal{C}_{2z} sends $(k_x, k_y, k_z) \rightarrow (-k_x, -k_y, k_z)$ such that $s_z \times \mathcal{T}$ is a valid symmetry operation that maps a k -point to itself on the $k_z = 0, \pi$ planes. When acting on a Bloch eigenstate of the Hamiltonian, $(s_z \mathcal{T})^2 = e^{-ik_z}$, a two-fold degeneracy is enforced on the entire $k_z = \pi$ plane. Thus, bands on the $k_z = \pi$ plane are two-fold degenerate in Te (SG 4). Furthermore, because points Z , A , D , and E lie on the nodal plane, only the isolated two-fold degeneracies at Γ , X , Y , and C are Kramers-Weyl nodes.

Conversely, three-fold screw rotations, which can only contain 1/3 or 2/3 fractional translations, cannot satisfy this algebraic constraint, and thus cannot obscure Kramers-Weyl points with nodal planes. In order to enforce $(s_{3z} \mathcal{T})^2 = -1$, s_{3z} must be capable of squaring to +1 (or should attain that value at least when being raised to an even power). However, as in these cases only $\mathcal{C}_{3z}^3 = e^{ik_z}$, there is no way for it to be combined with \mathcal{T} to

lead to a local Kramers theorem. Note that this stands in contrast to a 6_3 screw rotation $s_{6z} = \{C_{3z}|00\frac{1}{2}\}$, which can satisfy the required property. Consider IrSn₄ (SG 152) as an example (Figs. S1d-f), which has a 3_1 screw rotation $s_{3z} = \{C_{3z}|00\frac{1}{3}\}$, and nevertheless hosts Kramers-Weyl nodes at all of its TRIM points.

We can exhaustively deduce which of the possible screw axes allowed in 3D crystals support nodal planes when combined with time-reversal symmetry. Since nodal planes are enforced by anti-unitary symmetries which map every point of the plane to itself and square to -1 , for a screw rotation symmetry $s_{n,i}$, $i = x, y, z$, we require that taken to some power p , $s_{n,i}^p$ acts as a \mathcal{C}_2 rotation on the in-plane momenta. This ensures that the $k_i = \pi$ plane, which is left invariant by \mathcal{T} , can in principle be subject to a local constraint which derives from the nonsymmorphic symmetry, and limits the set of available screw rotations to those with $n = 2, 4, 6$. A second criterion we have to impose is $(s_{n,i}^p \mathcal{T})^2 = e^{ik_i q}$, where q is an odd integer, so that $(s_{i,n}^p \mathcal{T})^2 = -1$ on the $k_i = \pi$ plane enforces a local Kramers degeneracy. We therefore conclude that nodal planes can only be enforced by under the following screw symmetries: a two-fold rotation together with a $1/2$ lattice translation (2_1), a four-fold rotation with a $1/4$ translation (4_1), a sixfold rotation with a $1/6$ translation (6_1), as well as a sixfold rotation with a $1/2$ translation (6_3). We also observe that for all of these screw space group elements g , $g^p \equiv 2_1$, such that we arrive at a broad condition that in time-reversal-symmetric, double-valued (strong-SOC) space groups G , nodal planes are supported if $2_1 \in G$.

Consider as a final example the four-fold screw $s_{4z} = \{\mathcal{C}_{4z}| \frac{1}{4} \frac{3}{4} \frac{1}{4}\}$ in SG 214, which involves a quarter translation along the z direction, along with fractional transversal translations. We can form the operator

$$\begin{aligned} s_{4z}^2 &= e^{-i\left(\frac{\hat{k}_x}{4} + \frac{3\hat{k}_y}{4} + \frac{\hat{k}_z}{4}\right)} \mathcal{C}_{4z} e^{-i\left(\frac{\hat{k}_x}{4} + \frac{3\hat{k}_y}{4} + \frac{\hat{k}_z}{4}\right)} \mathcal{C}_{4z} \\ &= e^{-i\left(\hat{k}_x + \frac{\hat{k}_y}{2} + \frac{\hat{k}_z}{2}\right)} \mathcal{C}_{2z}, \end{aligned} \quad (\text{S6})$$

where at this level \hat{k}_i are still operators which are affected by crystal symmetry operations, such as \mathcal{C}_n rotations, as well as by \mathcal{T} , where we note in particular that $\mathcal{T}\hat{k}_i\mathcal{T}^{-1} = -\hat{k}_i$. This implies

$$\begin{aligned} (s_{4z}^2 \mathcal{T})^2 &= e^{-i\left(\hat{k}_x + \frac{\hat{k}_y}{2} + \frac{\hat{k}_z}{2}\right)} \mathcal{C}_{2z} \mathcal{T} e^{-i\left(\hat{k}_x + \frac{\hat{k}_y}{2} + \frac{\hat{k}_z}{2}\right)} \mathcal{C}_{2z} \mathcal{T} \\ &= e^{-ik_z} \mathcal{C}_{2z}^2 \mathcal{T}^2 = e^{-ik_z}, \end{aligned} \quad (\text{S7})$$

enforcing a Kramers degeneracy everywhere on the $k_z = \pi$ plane. It becomes clear that transversal lattice translations always cancel out. Note also that this calculation is equally valid in the limits of weak and strong SOC. We note that the focus of this section is purely on degeneracy, and not topology. We find in SI F that, in fact, these nodal planes may still be topologically nontrivial.

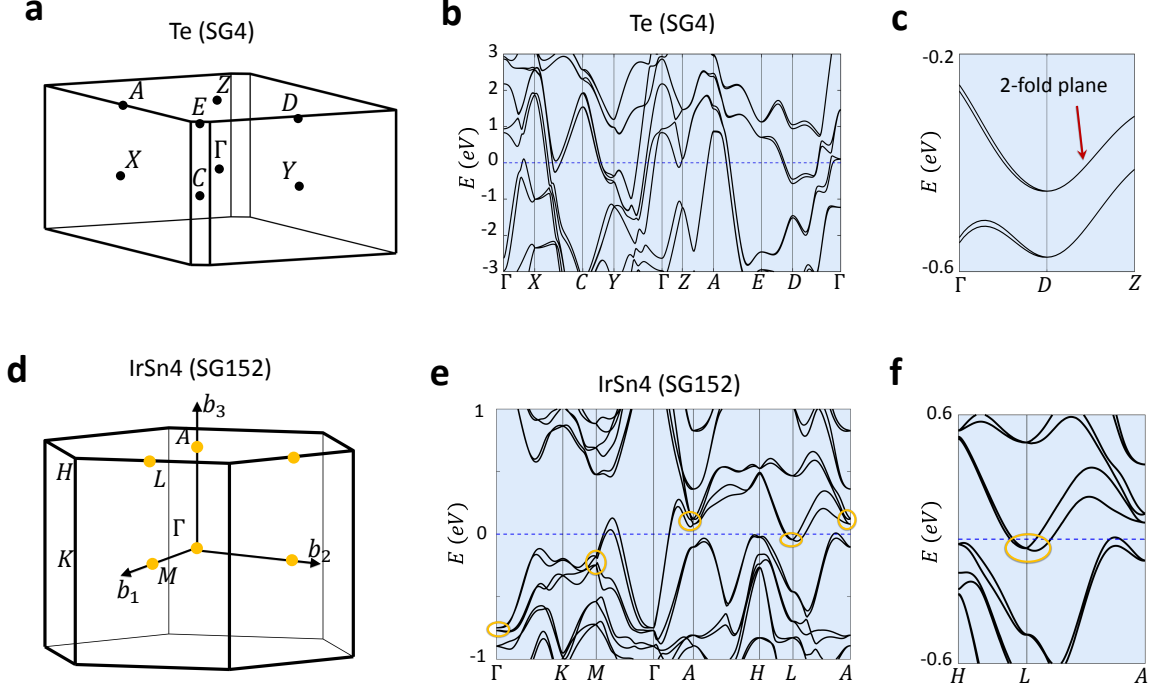


FIG. S1: **Kramers-Weyl nodes in nonsymmorphic chiral space groups.** (a) The bulk BZ and TRIM points of Te in SG 4. (b) The electronic band structure of Te along high-symmetry lines. (c) Bands in the vicinity of D . Along $D - Z$, which lies in the $k_z = \pi$ plane, bands are two-fold degenerate. (d) The BZ and TRIM points of SG 152. (e) The band structure of IrSn₄ in SG 152 along the high symmetry lines $H - L$ and $L - A$. (f) Bands passing through the L point at the zone boundary confirm that this TRIM hosts Kramers-Weyl fermions.

SI F. Topology of Nodal Surfaces in Nonsymmorphic Chiral Space Groups

Here we discuss the topological properties of nodal surfaces in the BZs of materials with nonsymmorphic chiral space groups. We here focus on the case of SG 19, the space group of the Kramers-Weyl compound Ag₂Se presented in the main text. As stated at the end of Sec. I, this space group has three orthogonal two-fold screw rotation symmetries

$$s_x = \{\mathcal{C}_{2x} | \frac{1}{2} \frac{1}{2} 0\}, \quad s_y = \{\mathcal{C}_{2y} | 0 \frac{1}{2} \frac{1}{2}\}, \quad s_z = \{\mathcal{C}_{2z} | \frac{1}{2} 0 \frac{1}{2}\}. \quad (\text{S8})$$

Acting on a Bloch state with momentum \mathbf{k} , these symmetries obey $(s_i \mathcal{T})^2 = e^{-ik_i}$ and for each $i = x, y, z$, the anti-unitary symmetry $s_i \mathcal{T}$ leaves momenta in the $k_i = 0, \pi$ plane invariant. In particular, on the $k_i = \pi$ planes they square to -1 and by Kramers pairing therefore imply a two-fold degeneracy on all surfaces forming the BZ boundary (instead of just the time-reversal invariant momenta), which may thus be viewed as a symmetry enforced nodal surface that may carry a topological charge. Figure S2a shows the location of the nodal surface in the BZ.

We note that at time-reversal symmetric momenta at which $k_i = \pi$ holds for exactly two k_i , the nonsymmorphic symmetries enforce a four-fold degeneracy. We can show this for, e.g., the point $\mathbf{k} = (\pi, \pi, 0)$ by studying the algebra

$$s_x s_y = -e^{i(k_y + k_z)} s_y s_x e^{ik_x} = -s_y s_x \quad (\text{S9})$$

that holds when acting on a Bloch state at $\mathbf{k} = (\pi, \pi, 0)$. At this point, time-reversal symmetry \mathcal{T} commutes with both s_y and s_x , which both square to $+1$ and mutually anticommute. This algebra enforces a four-fold degeneracy of every band at $\mathbf{k} = (\pi, \pi, 0)$, as highlighted in Refs. [4, 9]. These TRIM points are labeled with blue spheres in Fig S2a. At TRIMs for which only one or none of the $k_i = \pi$, the corresponding algebra is not satisfied and does not enforce higher degeneracies.

The nodal surfaces on the zone boundary in fact can also have a topological charge [10], which is given by the Chern number on an enclosing surface. The procedure for calculating this number is similar to enclosing a Weyl point with a sphere and calculating the Chern number of the eigenstates on the sphere. For a nodal plane, an example of such an enclosing surface can be formed by taking all of the points whose shortest distance to any point on the nodal surface is given by some infinitesimal number δ . As long as the spectrum on the

enclosing surface remains gapped under smooth deformations of the Hamiltonian, its Chern number is fixed, yielding an integer topological invariant for the nodal surface.

When time-reversal symmetry is imposed, the chiral charge of the nodal plane in SG 19 can only take odd-integer values. To see this, note that the surface enclosing the BZ boundary at fillings $\nu = 2, 6$ may also be viewed as a surface enclosing the rest of the BZ interior, including the Γ point, at which one Kramers-Weyl node resides [red dot in Fig. S2a]. Since these viewpoints only differ by an orientation reversal of the surface, the nodal surface Chern number has to be the opposite of that of the Weyl node at Γ , which is given by $C = \pm 1$, plus that of any other Weyl nodes in the BZ bulk. By time-reversal symmetry, such Weyl nodes in the BZ bulk may only appear in pairs with the same Chern numbers. For example, the black dots in Fig. S2a represent a pair of same charge Weyl points that are compatible with all the symmetries of SG 19 and time-reversal. In summary, in SG 19, because the Kramers-Weyl node at Γ has a chiral charge $\chi_\Gamma = \pm 1$, the nodal plane at the BZ has an odd-integer chiral charge χ_p , where $\chi_\Gamma - \chi_p \in 2\mathbb{Z}$ is the total chiral charge of other Weyl points in the bulk of the BZ at the same filling as the Kramers-Weyl fermion at Γ .

We now present an explicit tight-binding model for SG 19 displaying the aforementioned surface topology. A particularly natural realization of the symmetries given in Eq. (S8) is given by a simple fcc lattice with unit cell as shown in Fig. S2b, where the nearest-neighbor sites are related not by pure lattice translations, but instead by screw symmetries, such that the bravais lattice itself is still orthorhombic. To construct a tight-binding Hamiltonian, we begin with a model that includes all possible nearest-neighbor hoppings and SOC couplings, which has $6 \times 4 \times 4 = 96$ free parameters, as for each of the $\binom{4}{2} = 6$ possible bond pairings there are four directions along which an electron can hop with a spin rotation given by one of the three Pauli spin matrices σ_i , $i = x, y, z$ or the identity \mathbb{I} . Enforcing time-reversal and nonsymmorphic symmetries, we arrive at a model with 22 free parameters $a_1 \cdots a_{22}$ and a

Bloch Hamiltonian

$$H(\mathbf{k}) = \begin{pmatrix} 0 & h_{12}(\mathbf{k}) & h_{13}(\mathbf{k}) & h_{14}(\mathbf{k}) \\ h_{12}(\mathbf{k})^\dagger & 0 & h_{23}(\mathbf{k}) & h_{24}(\mathbf{k}) \\ h_{13}(\mathbf{k})^\dagger & h_{23}(\mathbf{k})^\dagger & 0 & h_{34}(\mathbf{k}) \\ h_{14}(\mathbf{k})^\dagger & h_{24}(\mathbf{k})^\dagger & h_{34}(\mathbf{k})^\dagger & 0 \end{pmatrix}, \quad (\text{S10})$$

$$h_{ij}(\mathbf{k}) = h_{ij}^{\text{hop}}(\mathbf{k})\sigma_0 + \mathbf{h}_{ij}^{\text{SOC}}(\mathbf{k}) \cdot \boldsymbol{\sigma},$$

where the hopping matrix elements are given by

$$\begin{aligned} h_{12}^{\text{hop}}(\mathbf{k}) &= a_1 + a_2 e^{-ik_x} + a_1 e^{-ik_z} + a_2 e^{-i(k_x+k_z)}, \\ h_{14}^{\text{hop}}(\mathbf{k}) &= a_3 + a_3 e^{-ik_y} + a_4 e^{-ik_z} + a_4 e^{-i(k_y+k_z)}, \\ h_{23}^{\text{hop}}(\mathbf{k}) &= a_4 + a_4 e^{-ik_y} + a_3 e^{+ik_z} + a_3 e^{-i(k_y-k_z)}, \\ h_{34}^{\text{hop}}(\mathbf{k}) &= a_2 + a_1 e^{+ik_x} + a_2 e^{-ik_z} + a_1 e^{+i(k_x-k_z)}, \\ h_{13}^{\text{hop}}(\mathbf{k}) &= a_5 + a_5 e^{-ik_x} + a_6 e^{-ik_y} + a_6 e^{-i(k_x+k_y)}, \\ h_{24}^{\text{hop}}(\mathbf{k}) &= a_6 + a_6 e^{+ik_x} + a_5 e^{-ik_y} + a_5 e^{+i(k_x-k_y)}, \end{aligned} \quad (\text{S11})$$

and the spin-orbit couplings by

$$\begin{aligned} \mathbf{h}_{12}^{\text{SOC}}(\mathbf{k}) &= i \begin{pmatrix} a_{11} + a_{12} e^{-ik_x} + a_{12} e^{-ik_z} + a_{12} e^{-i(k_x+k_z)} \\ a_{13} + a_{14} e^{-ik_x} + a_{13} e^{-ik_z} + a_{14} e^{-i(k_x+k_z)} \\ a_{15} - a_{16} e^{-ik_x} - a_{15} e^{-ik_z} + a_{16} e^{-i(k_x+k_z)} \end{pmatrix}, \\ \mathbf{h}_{14}^{\text{SOC}}(\mathbf{k}) &= i \begin{pmatrix} a_{17} + a_{17} e^{-ik_y} + a_{18} e^{-ik_z} + a_{18} e^{-i(k_y+k_z)} \\ a_{19} - a_{19} e^{-ik_y} - a_{20} e^{-ik_z} + a_{20} e^{-i(k_y+k_z)} \\ a_{21} + a_{21} e^{-ik_y} + a_{22} e^{-ik_z} + a_{22} e^{-i(k_y+k_z)} \end{pmatrix}, \\ \mathbf{h}_{23}^{\text{SOC}}(\mathbf{k}) &= i \begin{pmatrix} -a_{18} - a_{18} e^{-ik_y} - a_{17} e^{+ik_z} - a_{17} e^{-i(k_y-k_z)} \\ -a_{20} + a_{20} e^{-ik_y} + a_{19} e^{+ik_z} - a_{19} e^{-i(k_y-k_z)} \\ a_{22} + a_{22} e^{-ik_y} + a_{21} e^{+ik_z} + a_{21} e^{-i(k_y-k_z)} \end{pmatrix}, \\ \mathbf{h}_{34}^{\text{SOC}}(\mathbf{k}) &= i \begin{pmatrix} a_{12} + a_{11} e^{+ik_x} + a_{12} e^{-ik_z} + a_{11} e^{+i(k_x-k_z)} \\ -a_{14} - a_{13} e^{+ik_x} - a_{14} e^{-ik_z} - a_{13} e^{+i(k_x-k_z)} \\ -a_{16} + a_{15} e^{+ik_x} + a_{16} e^{-ik_z} - a_{15} e^{+i(k_x-k_z)} \end{pmatrix}, \\ \mathbf{h}_{13}^{\text{SOC}}(\mathbf{k}) &= i \begin{pmatrix} 0 \\ a_7 + a_7 e^{-ik_x} + a_8 e^{-ik_y} + a_8 e^{-i(k_x+k_y)} \\ a_9 + a_9 e^{-ik_x} + a_{10} e^{-ik_y} + a_{10} e^{-i(k_x+k_y)} \end{pmatrix}, \end{aligned} \quad (\text{S12})$$

$$\mathbf{h}_{24}^{\text{SOC}}(\mathbf{k}) = i \begin{pmatrix} 0 \\ -a_8 - a_8 e^{ik_x} - a_7 e^{-ik_y} - a_7 e^{+i(k_x-k_y)} \\ a_{10} + a_{10} e^{ik_x} + a_9 e^{-ik_y} + a_9 e^{+i(k_x-k_y)} \end{pmatrix}.$$

Calculating the Chern number of this Hamiltonian on a surface enclosing the BZ boundary formed by the planes $\{(k_x, k_y, \pi \pm \delta), (k_y, \pi \pm \delta, k_x), (\pi \pm \delta, k_x, k_y)\}$, $k_x, k_y \in (-\pi + \delta, \pi - \delta)$ with $\delta = 0.1$ for the generic model parameters quoted in the caption of Fig. S2, we confirm the above arguments and obtain $C = 1$.

In addition to Kramers-Weyl nodes at its TRIM points at fillings $\nu = 2, 6$, Eq. (S10) exhibits additional chiral fermions at half-filling, or $\nu = 4$. In Figs. S2 **c** and **d** we plot the bands of this model with and without the SOC terms, respectively. When SOC is negligible, this model exhibits a spin-degenerate eightfold chiral fermion at R with charge $C = -4$ and a pair of filling-enforced spinless double-Weyl points along ΓX , each with charge $C = 2$, in agreement with the results of Refs. [11–13]. When SOC is reintroduced, these points split, but the filling-enforced gaplessness at $\nu = 4$ is still preserved by the spinful symmetries of SG 19 [4, 14]. The chiral fermion at R splits into two nonsymmorphic, zone-edge double-Weyl points [15, 16] (SI **N**), each with charge $C = -2$. More interestingly, the moveable-but-unremovable spinless double-Weyl points along ΓX split into four conventional $C = 1$ Weyl points in the $k_y = 0$ plane. To understand this splitting, we observe that the conservation of chiral charge requires that the sum of the Chern numbers of the nodal degeneracies in the vicinity of previous spinless double-Weyl points is $+2$, and note that the spinful screw symmetries cannot preserve a double-Weyl point along ΓX [6]. Therefore, upon introducing SOC, each spinless double-Weyl point will either split into two Weyl points along the screw line, or, more generically and as occurs in our model, two Weyl points in either of the $k_{y,z} = 0$ planes. Most interestingly, as the spinless double-Weyl points are filling-enforced [4, 14], then the conventional Weyl fermions in the $k_y = 0$ plane of our model, while not characterized by any symmetry eigenvalues, are *also* filling-enforced. This indicates that the large-SOC phase of Eq. (S10) is the rare example of a filling-enforced semimetal whose minimal band connectivity [4, 5] is connected through a *low-symmetry BZ plane*.

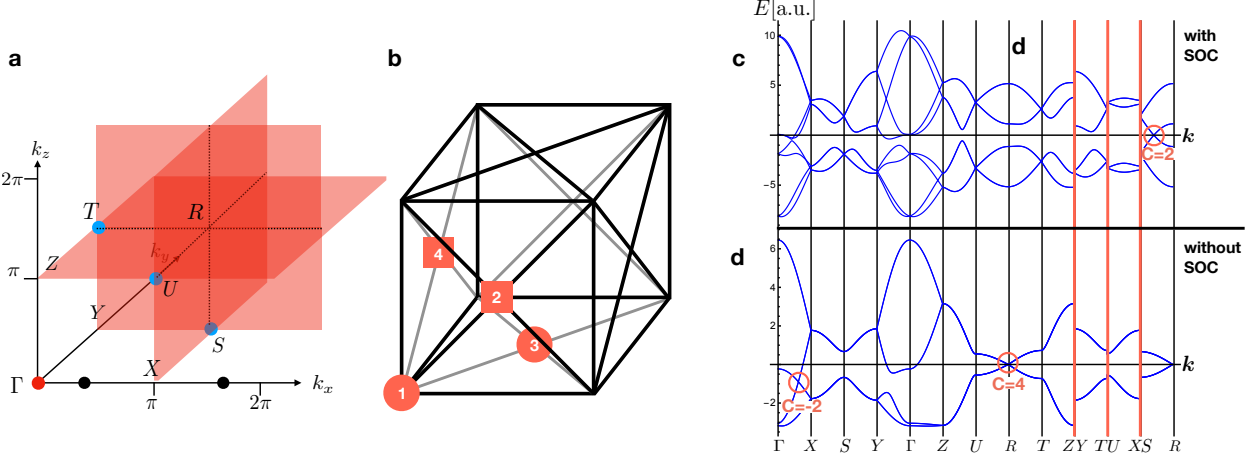


FIG. S2: Nodal surfaces in SG 19. (a) BZ for SG 19, with a nodal surface (red) at fillings $\nu \in 2 + 4\mathbb{Z}$, on which at the zone edges all bands are two-fold degenerate. At the same fillings, the minimal connectivity of SG 19 also displays a two-fold-degenerate Kramers-Weyl fermion (red dot) at Γ . Blue spheres indicate the four-fold-degenerate points that occur at the intersections of two nodal planes. (b) Unit cell of the lattice on which the tight-binding Hamiltonian (S10) is defined. (c) Band structure of the tight-binding Hamiltonian (S10) incorporating the effects of SOC, plotted with parameter values $a_1 \dots a_{22} = (0.593237, 0.258583, 0.547374, 0.27201, 0.596372, 0.959641, 0.945241, 0.191225, 0.557652, 0.583338, 0.461802, 0.00999746, 0.862848, 0.592332, 0.781321, 0.791785, 0.760452, 0.394747, 0.860525, 0.145271, 0.25431, 0.308917)$. The fourfold degeneracies along the SR carry Chern number $C = 2$; there are four other Weyl points with $C = -1$ in the $k_y = 0$ plane that are not visible in this plot. (d) Band structure of Eq. (S10) with all of the SOC terms set to zero. There is a spin-degenerate eightfold chiral fermion at R with charge $C = -4$ and a pair of filling-enforced spinless double-Weyl points along ΓX , each with charge $C = 2$, in agreement with the results of Refs. [11–13]. Upon the reintroduction of SOC, all of these points split, but the system remains gapless at $\nu = 4$. This indicates that the four conventional spinful Weyl points at $k_y = 0$ are in fact *filling-enforced* [4, 14]; despite not being characterized by symmetry eigenvalues, they enforce the minimal band connectivity [4, 5] of SG 19 *through a BZ plane*.

SI G. Kramers-Weyl Nodes in Achiral Space Groups

In this section, we discuss the possibility of realizing Kramers-Weyl nodes in achiral space groups with mirror planes. As noted in the main text, any form of roto-inversion is sufficient to remove the geometric “handedness” of a chiral lattice resulting in a non-chiral (achiral) crystal. As a Weyl node and its mirror partner have opposite chiral charge, as shown in Fig. S3a, Weyl nodes cannot be stabilized on a mirror plane. For this reason, Kramers points in achiral space groups, which in most cases are on mirror planes, cannot be chirally charged. To illustrate this, we show in Fig. S3b a hexagonal lattice with mirror planes parallel to unit vectors b_1 and b_2 , in which we observe topologically trivial Kramers points (black circles) in the BZ. However, if a TRIM does not reside on a mirror plane, then it is still possible for it to realize a Kramers-Weyl node, even in an achiral crystal (as long as inversion symmetry \mathcal{I} is not also present). In Fig. S3c we illustrate a system that has mirror planes not parallel to its unit vectors b_1 and b_2 . As shown in Fig. S3c, the Kramers pairs at M and L are indeed Kramers-Weyl nodes. Note that Γ , which is intersected by all the mirror planes, does not possess a Kramers-Weyl node.

To study this case in a real crystal system, we use BiTeI (SG 156) as an example, which is famous for its giant Rashba splitting at its A points. The bulk BZ of BiTeI and its high-symmetry points are shown Fig. S3d, and its electronic band structure along high-symmetry directions is shown in Fig. S3e. Zoomed-in views of the bands near TRIMs Γ , A , L , and M are shown in Figs. S3f,g, and reveal that bands along $\Gamma - A$ are two-fold degenerate. However, at M and L we observe isolated two-fold degeneracies that are linearly dispersing along all directions in momentum space, and are thus Kramers-Weyl nodes. Conversely, Kramers-Weyl nodes are notably absent at Γ and A . We note that because the crossings at M and L in BiTeI are too far away from the Fermi level to be enclosed by Fermi surfaces, the Kramers-Weyl nodes at M and L have no effect on the low energy physics.

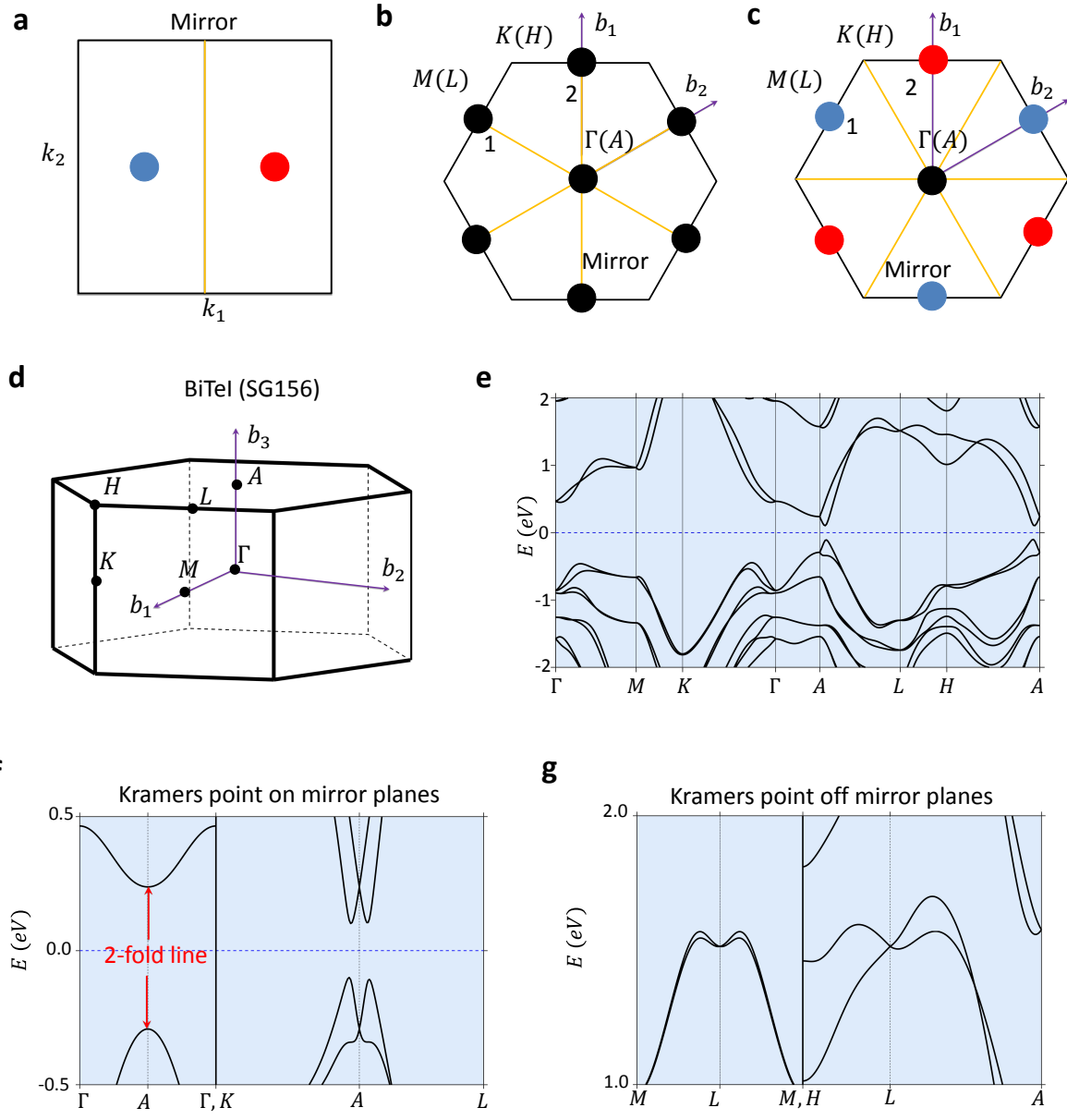


FIG. S3: **Kramers points in an achiral group.** (a) A Weyl node and its mirror partner hold opposite chiral charges, which are represented by the blue and red circles. The mirror plane is shown in yellow. (b) A hexagonal lattice whose Kramers points are all on the mirror plane. In such systems, no Kramers pairs possess chiral charge and, therefore, all are shown in black. (c) A hexagonal lattice with mirror planes that do not intersect its TRIMs exhibits Kramers-Weyl nodes at L and M (d,e). The bulk BZ and electronic band structure of BiTeI (SG 156). (f,g) The band structures in the vicinity of TRIMs for BiTeI.

SI H. Fermi Surface Analysis of Kramers-Weyl Materials

Comparing the Fermi surface evolution of Kramers-Weyl metals to band-inversion Weyl semimetals, there is a notable contrast in topological character. Consider the electronic band structure of a band-inversion Weyl semimetal, shown in Fig. S4a, in which the energy levels of interest for a Fermi surface analysis are labeled as E_1 , E_2 , and E_3 and the critical points that correspond to Lifshitz transitions are marked in yellow. Starting at an energy level that is well above the band-inversion Weyl nodes, E_3 , we observe that the bulk Fermi surface (whose boundary is defined by the black closed contour) encloses the projection of both oppositely chiral charged Weyl nodes and is, therefore, topologically trivial, as shown in the leftmost panel of Fig. S4b. Lowering the energy level past the top critical point moves the Fermi surface through a Lifshitz transition. At energy level E_2 , which is slightly below the pair of Weyl nodes, we observe that the initial Fermi surface splits into two. Generally, at energies between the two Lifshitz transition points, each projected Weyl node is enclosed by its own Fermi surface and therefore, each individual surface is topologically nontrivial, as shown in middle panel of Fig. S4b. The yellow arrows in Fig. S4b indicate the direction of Berry flux emanating from each projected Weyl node and nontrivial Fermi surface. As the energy level is further lowered, the Fermi surface undergoes a second Lifshitz transition. At energy level E_1 , which is close to E_3 , a single Fermi surface again encloses both projected oppositely chiral charged Weyl nodes, and is therefore topologically trivial, as shown in the rightmost panel of Fig. S4b.

Performing a similar evaluation on the model Kramers-Weyl metal in symmorphic chiral space groups, the Fermi surface evolution is drastically different. The cartoon of the electronic structure of a Kramers-Weyl material is shown in Fig. S4c. Starting at E_1 , we observe two concentric Fermi surfaces around the projected Kramers-Weyl nodes at the BZ center. Unlike the Fermi surface of a band-inversion Weyl semimetal, we instead here observe two distinct, oppositely chiral charged Fermi surfaces enclosing the projected Kramers-Weyl node at the zone center. As shown in Fig. S4 d, the inner Fermi surface is formed by the upper cone of the Kramers-Weyl node, while the outer Fermi surface is formed by the lower cone. As the energy level is increased to E_2 , the nontrivial outer Fermi surface expands towards the zone boundary. At E_3 , each Kramers-Weyl node has its own individual nontrivial Fermi surface. The topological properties of these Kramers-Weyl Fermi surfaces therefore

differ strongly from those observed or predicted in previous band-inversion Weyl semimetals. Furthermore, the energy window corresponding to the presence of topologically nontrivial Fermi surfaces in Kramers-Weyl metals, mainly determined by the bandwidth in the limit of vanishing SOC, can be in the energy range of multiple eV. This property makes experimental observation of topological surface physics in Kramers-Weyl metals promisingly plausible.

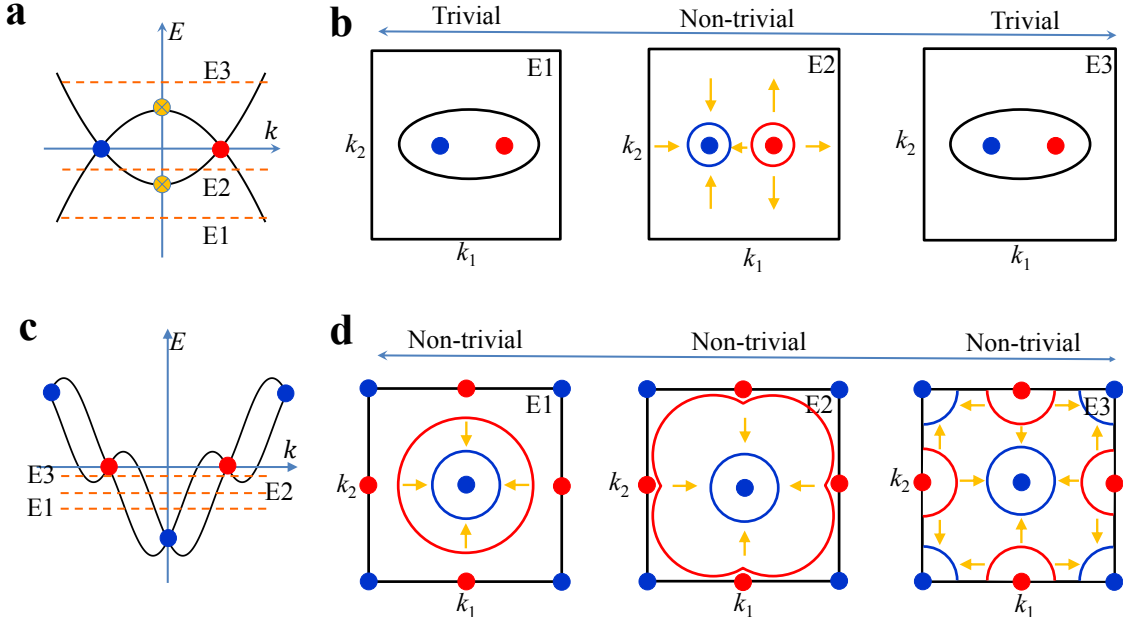


FIG. S4: Topological Fermi surface of Kramers-Weyl nodes. (a) The electronic band structure of a conventional band-inversion Weyl semimetal. The blue and red colors represent Weyl nodes of opposite chiral charge. The yellow colors indicate the points where a Lifshitz transition occurs. (b) The sequence of Fermi surfaces shown are for energy levels E1, E2, and E3, which are annotated in panel (a). The red and blue coloring of the Fermi surfaces indicates a positive or negative Chern number, respectively. The net chiral charge enclosed by the black Fermi surface is zero and therefore it is topologically trivial. The yellow arrows illustrate the flow of Berry curvature from each topologically nontrivial Fermi surface. The Fermi surface of a band-inversion Weyl semimetal is topologically nontrivial for the energy window defined by the degree of band-inversion, which is typically small. (c) The electronic band structure of a typical Kramers-Weyl metal. (d) The Fermi surface for energy levels E1, E2, and E3, annotated in panel (c). The Fermi surface of a Kramers-Weyl metal remains topologically nontrivial from the bottom to the top of the bands. Thus, the energy window corresponding to a topologically nontrivial Fermi surface for a Kramers-Weyl metal can be as large as multiple eV.

SI I. Fermi Arcs in Kramers-Weyl Metals

The unique bulk Fermi pockets of Kramers-Weyl Fermions indicate that the appearance of surface states in Kramers-Weyl metals also differs significantly from in band-inversion Weyl semimetals. In this section, we show the distinct distribution of topological Fermi arcs in a Kramers-Weyl metal, using our tight-binding model of SG-16. In Fig. S5a we show the distribution of Kramers-Weyl nodes at the bulk TRIMs. To study the emerging Fermi arc surface states, we consider the projection of Kramers-Weyl nodes onto the (110)-surface. In Fig. S5b we show that on this surface, each TRIM has a projected Kramers-Weyl node with chiral charge ± 2 . Pictured in Fig. S5c, we first calculate the bulk and (110)-surface states for when the SOC strength t^s is smaller than lattice hopping strength t^1 . Examining in Fig. S5d a constant energy contour at $E = -0.5$ eV reveals that the majority of the projected Kramers-Weyl nodes are covered by bulk pockets that consequently conceal their Fermi arc surface states. However, the projected Kramers-Weyl nodes at \bar{X} and \bar{M} are not covered by the projected bulk pockets and, as shown in Fig. S5d, exhibit connecting Fermi arc surface states. To check if the surface states around \bar{M} are consistent with the expected chiral charge projection, we calculate the energy dispersion around a closed path encircling \bar{M} , as displayed in Fig. S5e. We observe two chiral surface states dispersing along the same \mathbf{k} direction, confirming that the path defined in Fig. S5d encloses a projected Kramers-Weyl node of chiral charge +2.

To study the effect of adiabatically increasing SOC, we present in Fig. S5f the electronic band structure of our SG-16 tight-binding model for t^s much larger than t^1 . As discussed earlier, irrespective of SOC strength, the Kramers-Weyl nodes remain permanently pinned to the TRIMs under the preservation of \mathcal{T} symmetry. We find that the increase of SOC extensively distorts the bulk bands, allowing for Fermi arcs to be observed over a wider section of the projected surface BZ. Although the Kramers-Weyl nodes are fixed in momentum space, they are still free to move in energy when SOC is tuned. The resulting constant energy contour at $E = -0.5$ eV for the (110) surface is shown in Fig. S5g. Under high-SOC conditions, the projections of Kramers-Weyl nodes are no longer concealed by the projections of bulk pockets and the Fermi arc connectivity becomes easily resolvable. Proceeding as before, the energy-dispersion calculation around a path encircling \bar{M} reveals two co-propagating chiral modes, and again confirms that the enclosed projected Kramers-Weyl

node has a +2 chiral charge. In general, all of the TRIMs in symmorphic chiral crystals are guaranteed to host Kramers-Weyl nodes, and therefore these systems, if SOC is very large, may host a novel topological Weyl metallic phase with large and well-separated Fermi arcs, similar to the unconventional chiral semimetallic phase predicted in β -RhSi [17].

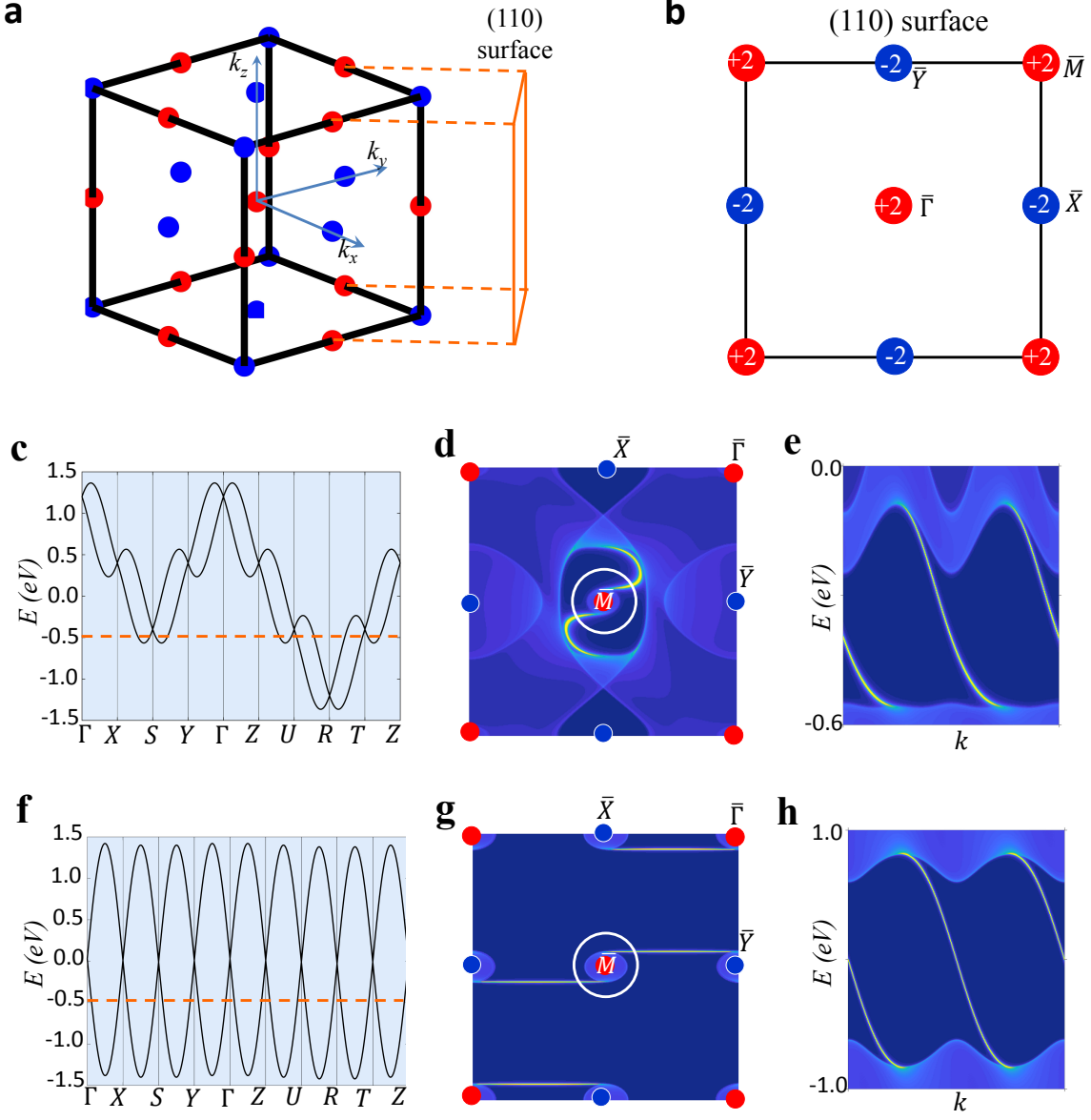


FIG. S5: Fermi arcs in a Kramers-Weyl metal. (a) The chiral charge distribution of Kramers-Weyl nodes in the bulk BZ of SG-16. (b) The projected chiral charge on the (110) surface. The number labeled in each red and blue marking represents the projected chiral charge at that point. (c) The electronic band structure of a Kramers-Weyl metal in SG-16 from the tight-binding model presented in this paper, set with t_s smaller or of the same order as t_l (d) The surface states of the (110) surface at -0.5 eV. Indicated in panel (c) by the orange-dashed line is the energy-level corresponding to (d). (e) Energy-dispersion calculation of surface states along the path defined by the white circles enclosing the \bar{M} -point. The number of chiral surface states is consistent with the projected chiral charge.

FIG. S5: (f) We adiabatically change the electronic band structure of the Kramers-Weyl metal by increasing the SOC interaction term t_s relative to the lattice hopping term t_l . Panel (f) shows the band structure when t_s is much larger than t_l . (g, h) The surface states calculations from the bands in panel (f) at -0.5 eV.

SI J. Additional Kramers-Weyl Materials

Here, we present in Figs. S6-S9 additional material candidates that feature Kramers-Weyl fermions. These materials are either candidate Kramers-Weyl metals with clean Fermi surfaces (Figs. S6 and S8), or are small-gap insulators with Kramers-Weyl fermions near their Fermi levels (Figs. S7 and S9). Among them, We identify 16 additional chiral materials platforms for the observation of Kramers-Weyl-enabled quantized photocurrent and the chiral and gyrotropic effects: CsCuBr₃(#10184) in SG-20, BaAg₂SnSe₄(#170856) in SG-23, β -NbO₂ (#35181) in SG-80, Ag₃SbO₄(#417675) in SG-91, MgAs₄(#1079) in SG-92, m-Cu₂S(#16550) in SG-96, Ta₂Se₈I(#35190) in SG-97, CdAs₂ (#16037) in SG-98, β -Ag₃IS(#93431) in SG-146, Tl₂TeO₆(#4321) in SG-150, SrIr₂P₂(#73531) in SG-154, m-Bi₂O₃(#27152) in SG-197, K₂Sn₂O₃(#40463) in SG-199, and Ag₃Se₂Au(#171959) in SG-214 are similar chiral crystals with narrow band gaps, such that moderate doping may allow the isolation of a Kramers-Weyl node at the Fermi level; BaCu₂Te₂O₆Cl₂ (#85786) in SG-4 and Ca₂B₅Os₃(#59229) in SG-5 are semimetallic crystals which each have Fermi pockets that enclose a single Kramers-Weyl node at intrinsic doping.

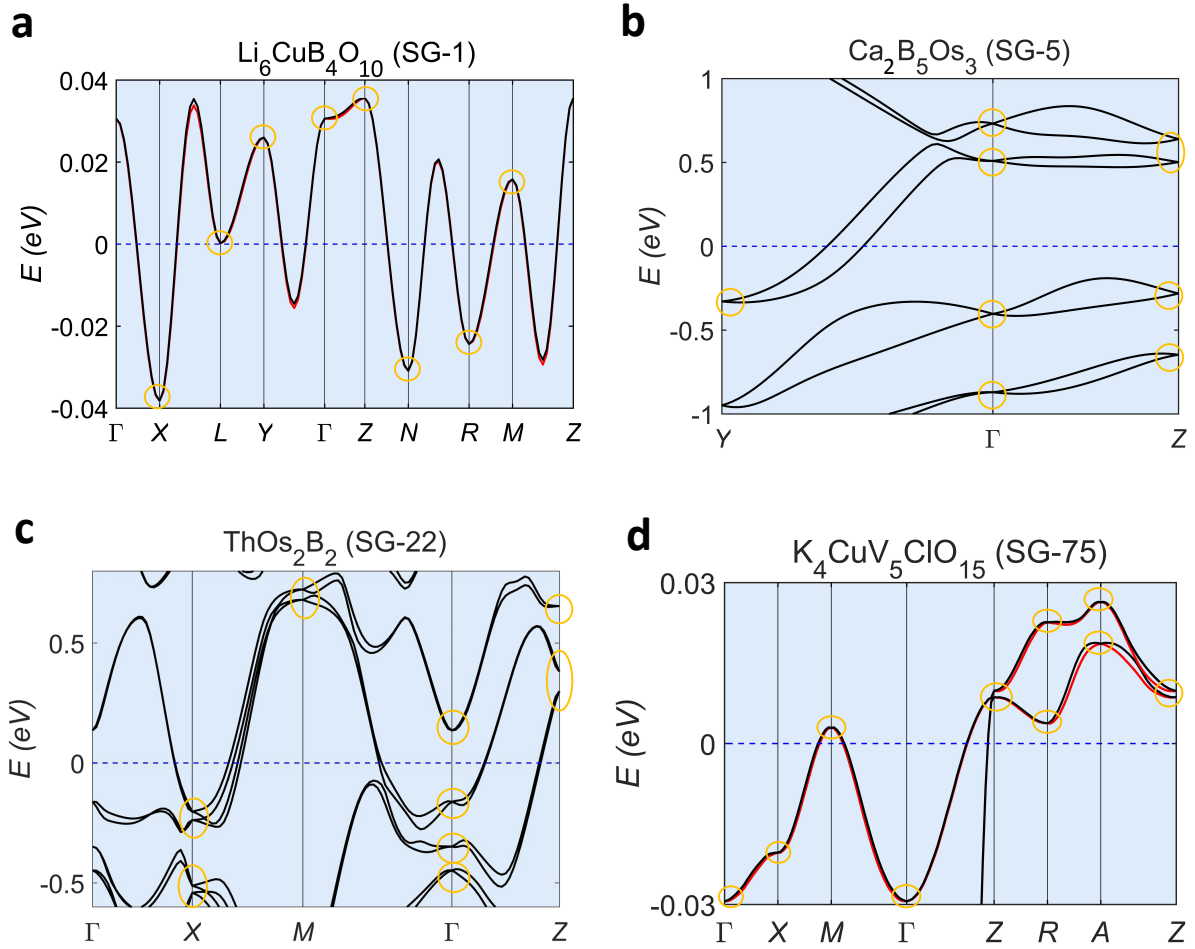


FIG. S6: Candidate Kramers-Weyl metals in symmorphic chiral space groups.

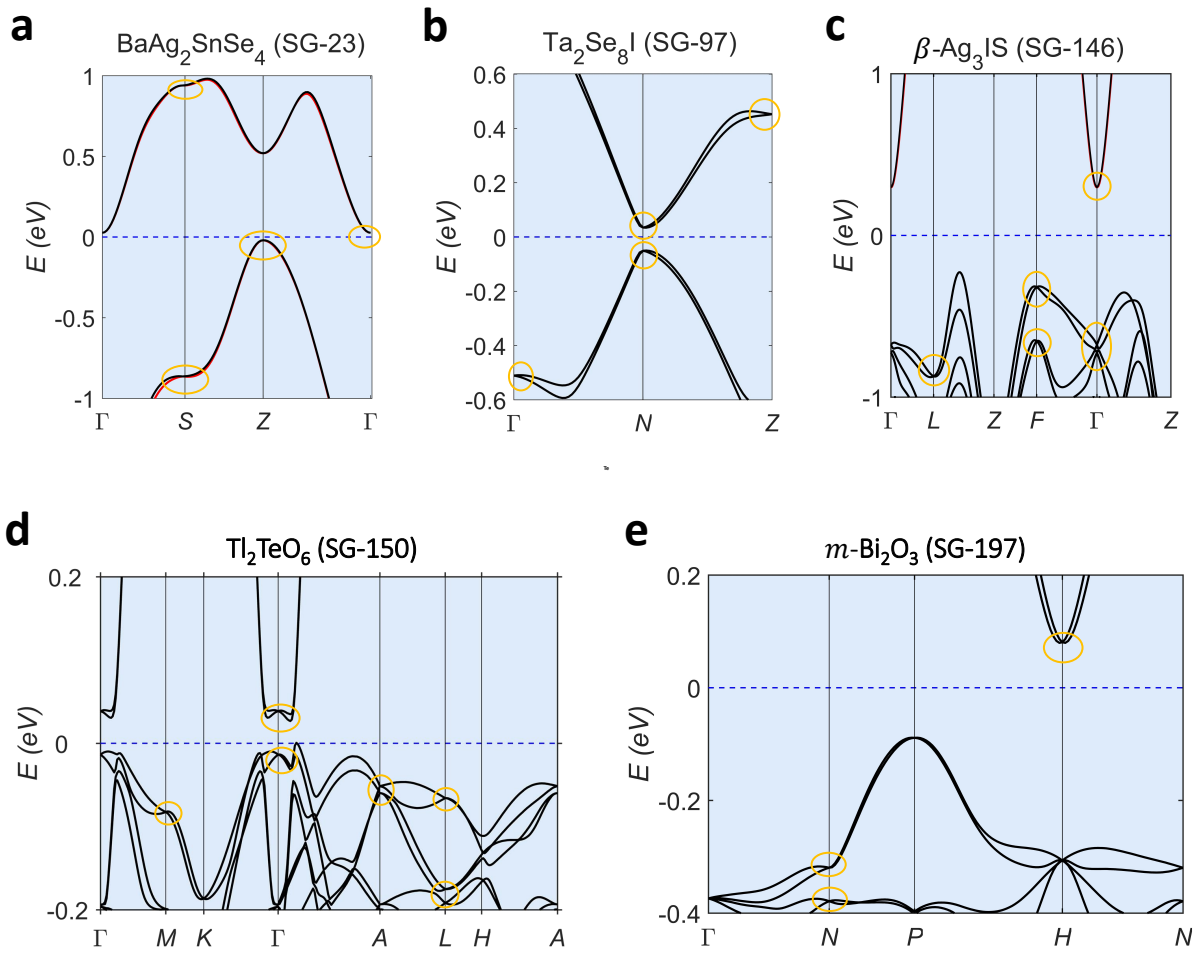


FIG. S7: Small-gap insulators in symmorphic chiral space groups with Kramers-Weyl fermions near their Fermi levels.

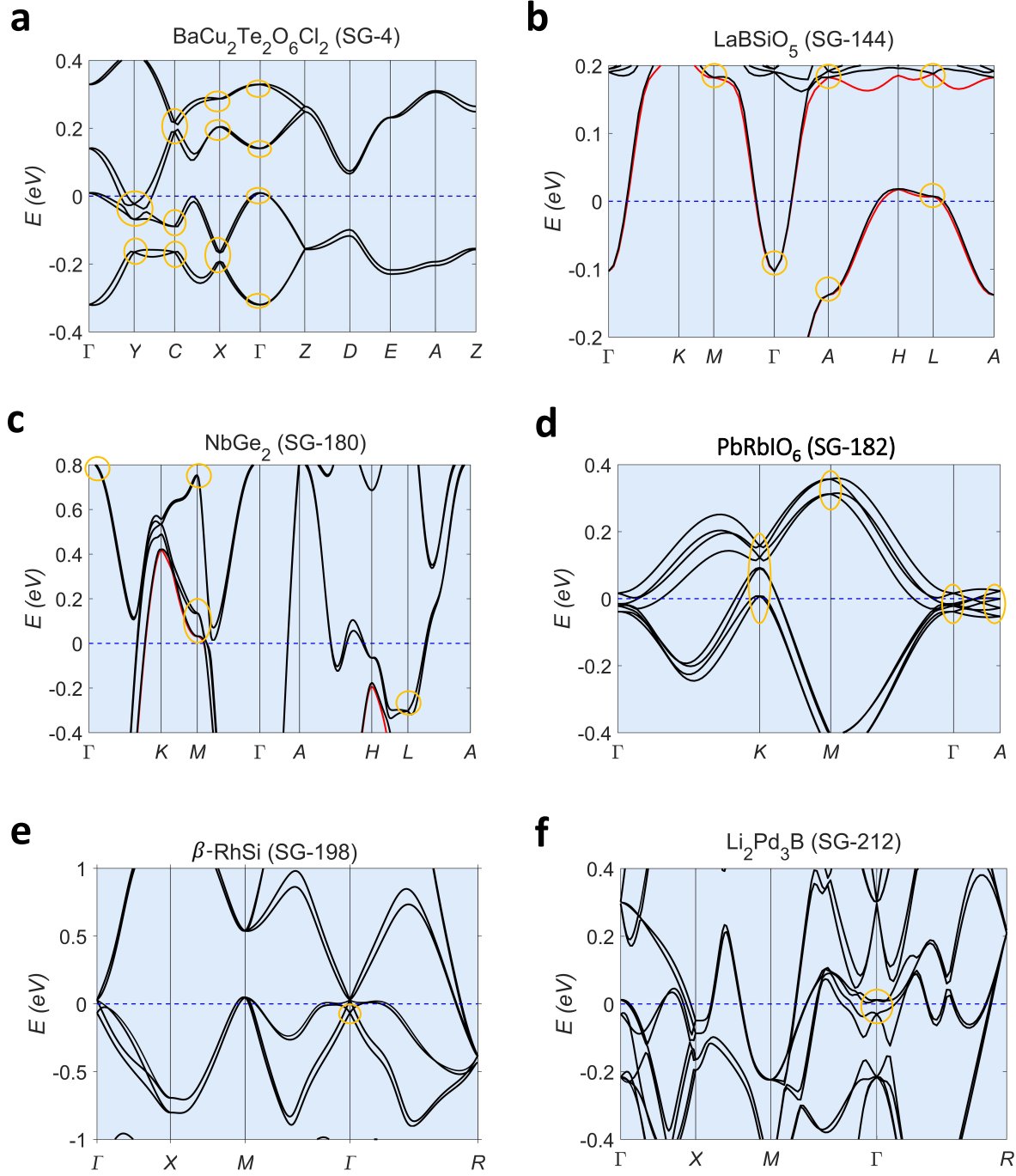


FIG. S8: **Candidate Kramers-Weyl metals in nonsymmorphic chiral space groups.** We note that $\beta\text{-RhSi}$ is also a chiral unconventional fermion semimetal [17].

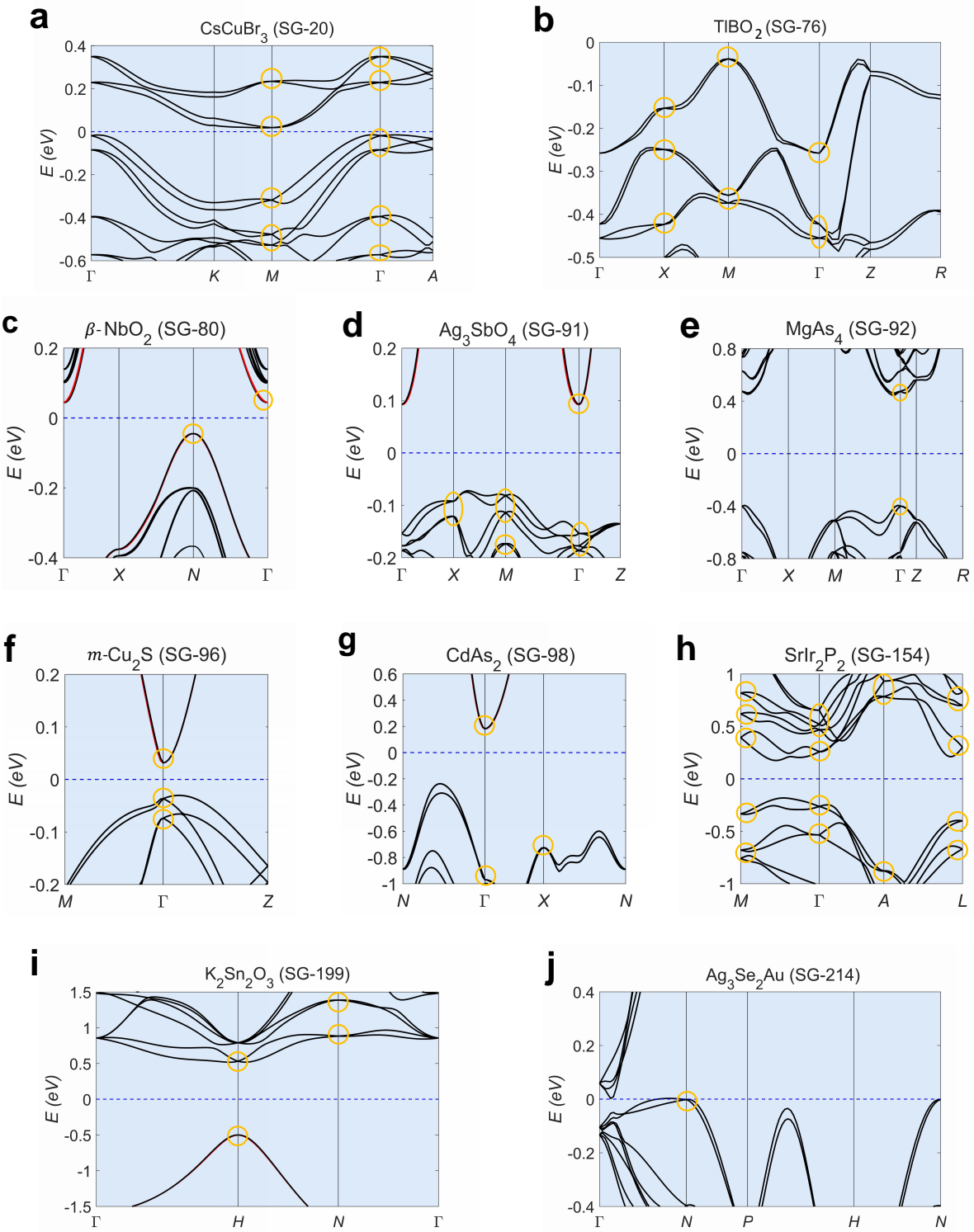


FIG. S9: Small-gap insulators in nonsymmorphic chiral space groups with Kramers-Weyl fermions near their Fermi levels.

	Weyl nodes	$k_x(\pi/a)$	$k_y(\pi/a)$	$k_z(\pi/c)$	Chirality	Number
W_1^K	0.000	0.000	0.000	-1	1	
W_2^K	0.500	0.000	0.5000	+1	2	
W_3^K	1.000	0.5000	0.500	+1	2	
W_4^K	0.500	0.500	0.000	+1	1	
W_5^K	0.500	0.500	1.000	+1	1	
W_6^K	1.000	1.000	1.000	+1	1	
W_1^I	0.5	0.5	0.5	+1	2	
W_2^I	0.3831	0.5493	0.4214	-1	8	

TABLE S4: **Weyl node distribution in the BZ of AgBi(Cr₂O₇)₂.** Kramers-Weyl fermions are labeled as W_m^K , and conventional band-inversion-generated Weyl nodes are noted as W_n^I

SI K. Weyl Nodes Distribution in AgBi(Cr₂O₇)₂

In Table S4, we list for reference the locations of both the conventional band-inversion and Kramers-Weyl fermions in AgBi(Cr₂O₇)₂ in SG 79, obtained from first-principles calculations.

SI L. Theory for Novel Spin Texture of Kramers-Weyl fermions

In this section we characterize the spin texture of Fermi surfaces enclosing Kramers-Weyl fermions in momentum space. We will first treat the case in which there are no other bands except for the two that participate in the crossing at the Kramers-Weyl node. Remember that conventional band-inversion Weyl fermions can be described in terms of a pseudo-spin degree of freedom that involves superpositions of physical spin and orbital degrees of freedom. In contrast, for Kramers-Weyl fermions we define below a limit in which the pseudo-spin coincides with the physical spin and we give symmetry conditions under which the spin and the momentum around a Kramers-Weyl point are rigidly locked to one another. The most general effective two-band $\mathbf{k} \cdot \mathbf{p}$ Hamiltonian of a Kramers-Weyl fermion (taken as an

expansion about any given TRIM point, e.g., Γ) acts solely on physical spin. It is given by

$$\mathcal{H}_{\mathbf{k}\cdot\mathbf{p}} = \mathbf{d}_k \cdot \boldsymbol{\sigma}, \quad d_j(\mathbf{k}) = \sum_{i=x,y,z} k_i A_{i,j}, \quad (\text{S13})$$

where $\boldsymbol{\sigma}$ is the vector of physical spin Pauli matrices and A is a real symmetric 3×3 matrix. Note that this form is valid absent spatial symmetries, which further constrain the values of the matrix A and will be considered later in this section. Note also that a \mathbf{k} -linear term that is proportional to the identity matrix is not allowed by time-reversal symmetry. Such terms lead to a ‘tilting’ of Weyl cones on low-symmetry points in the Brillouin zone. Consider now a spherical surface Σ in momentum space that encloses the Kramers-Weyl node. The eigenstates for the momenta on the surface organize into two bands that are in general separated by a bandgap everywhere (since the only enforced crossing occurs at $\mathbf{k} = 0$). The Chern number of any two-dimensional Hamiltonian of the form given in Eq. (S13), as parameterized by \mathbf{d}_k , $\mathbf{k} \in \Sigma$, can be written as

$$C = \frac{1}{4\pi} \int_{\Sigma} dk_x dk_y \frac{1}{|\mathbf{d}_k|^3} \mathbf{d}_k \cdot \left(\frac{\partial \mathbf{d}_k}{\partial k_x} \times \frac{\partial \mathbf{d}_k}{\partial k_y} \right). \quad (\text{S14})$$

This formula evaluates how often the unit vector $\hat{\mathbf{d}}_k \equiv \mathbf{d}_k / |\mathbf{d}_k|$ covers its target space, the sphere S^2 , as we vary \mathbf{k} across the Brillouin zone. Without further spatial symmetries, Kramers-Weyl fermions have $C = \pm 1$. In this case, we know that $\hat{\mathbf{d}}_k$ takes every value on S^2 at least once. In addition, we know from Eq. (S13) that the energetically higher band $|u^+(\mathbf{k})\rangle$ will have its spin expectation value $\langle \sigma \rangle^+ \equiv \langle u^+(\mathbf{k}) | \boldsymbol{\sigma} | u^+(\mathbf{k}) \rangle$ aligned parallel to $\hat{\mathbf{d}}_k$ at every momentum, while the expectation value $\langle \sigma \rangle^-$ in the lower band $|u^-(\mathbf{k})\rangle$ is always antiparallel to $\hat{\mathbf{d}}_k$. This is just due to the fact that in these states, which are by definition eigenstates of the Hamiltonian, we have

$$\langle \mathcal{H}_{\mathbf{k}\cdot\mathbf{p}} \rangle^{\pm} = \mathbf{d}_k \cdot \langle \boldsymbol{\sigma} \rangle^{\pm}, \quad (\text{S15})$$

and we know that the states $|u^{\pm}(\mathbf{k})\rangle$ maximize (minimize) the expectation value $\langle \mathcal{H}_{\mathbf{k}\cdot\mathbf{p}} \rangle$. We can thus conclude that within this two-band model for Kramers-Weyl fermions, the expectation value of physical spin sweeps out the entire unit sphere S^2 on Fermi surfaces enclosing the Weyl node. However, for conventional band-inversion Weyl fermions, the spin only sweeps parts of the unit sphere S^2 .

In the presence of rotational symmetries, which can be two-, three-, four- or six-fold in a crystal, we have spin-momentum locking in addition: consider without loss of generality the z

direction as rotational axis. Then for $\mathbf{k} = k_z \hat{\mathbf{e}}_z$, $\langle u(\mathbf{k}) | \sigma_i | u(\mathbf{k}) \rangle$ is only nonzero for $i = z$, since any other direction of the spin expectation value, which would not be parallel to the z -axis, would break the rotational symmetry. Therefore, in the case of three mutually orthogonal rotation axes, Kramers-Weyl fermions display perfect spin-momentum locking along these axes. The chiral point groups with this property all contain 222, and are therefore 222, 422, 622, 23, and 432 (SI **B**). In this case, the Chern number can be described by even more straightforward properties of the spin texture. Specifically for a $C = +1$ Kramers-Weyl node, the spin either points outward along all three principal directions or it points outward along one direction but inward along the other two directions; for a $C = -1$ Kramers-Weyl node, the spin either points inward along all three principal directions or it points inward along one direction but outward along the other two directions(Figs. S10 **a** and **b**). Note that this is different from conventional Weyl fermions which appear on low-symmetry points in the Brillouin zone away from any rotational axis(Fig. S10 **c** and **d**).

Note that this argument holds strictly only in the case of two bands. In a real electronic structure, the bands that cross at a Kramers-Weyl node are however never completely energetically isolated from other bands (which themselves form Kramers-Weyl nodes at the TRIMs). Therefore, hybridization can in principle occur and destroy the pure spin character of Fermi surfaces enclosing the Weyl node. In particular, let m be the separation in energy of a particular Kramers-Weyl node and the energetically closest next node (which may lie lower or higher in absolute energy). Then, the deviation of the actual spin texture from the ideal two-band case described above (for a Fermi surface enclosing the Weyl node with a sufficiently small radius) is small as long as $m \gg c$, where c is the strength of SOC. This implies that Kramers-Weyl nodes originating from two-dimensional *spinless* corepresentations (*i.e.*, fourfold degeneracies including spin, with vanishing SOC) will necessarily have strong interband coupling and cannot realize this pure spin character. Specifically, when SOC is reintroduced, these spinless nodes will split in energy, but only with a splitting on the scale of the SOC $m \approx c$. These higher-dimensional spinless degeneracies comprise the set of weak-SOC corepresentations of the chiral point groups that have complex rotation eigenvalues; they are enumerated in SI **C**.

To demonstrate our theory, we show the spin texture of a $C=+1$ Kramers-Weyl fermion in Ag₂Se (Figs. S10 and S11). The physical spin of the Kramers-Weyl fermion in Ag₂Se indeed sweeps out the full Bloch sphere. Further, because Ag₂Se is in SG 19 (C_2 rotations

along k_x , k_y , k_z axes), spin-momentum locking is observed along all three principle axes, $\mathbf{S}_{(k,0,0)} \parallel \mathbf{x}$, $\mathbf{S}_{(0,k,0)} \parallel \mathbf{y}$, $\mathbf{S}_{(0,0,k)} \parallel \mathbf{z}$, where \mathbf{S}_k is the spin expectation value of the occupied band at momentum \mathbf{k} . From the sign of $\mathbf{S}_{(k,0,0)} \cdot \mathbf{x}$ etc., we can thus compute the Chern number $C^{\text{Kramers-Weyl}} = -\text{sign}(k)\text{sign}(\mathbf{S}_{(k,0,0)} \times \mathbf{S}_{(0,k,0)} \cdot \mathbf{S}_{(0,0,k)}) = +1$. By contrast, the spin of the regular Weyl fermions in TaAs does not sweep out the entire unit sphere, does not show spin momentum locking, and does not correspond to its Chern number.

Therefore, the spin of Kramers-Weyl fermion (1) must sweep out the entire unit sphere; (2) show spin-momentum locking in the presence of additional rotational symmetry; and (3) can be used to measure the Chern number $C^{\text{Kramers-Weyl}} = -\text{sign}(k)\text{sign}(\mathbf{S}_{(k,0,0)} \times \mathbf{S}_{(0,k,0)} \cdot \mathbf{S}_{(0,0,k)})$. These are unique properties of the Kramers-Weyl fermions which are absent for a regular band inversion Weyl semimetal.

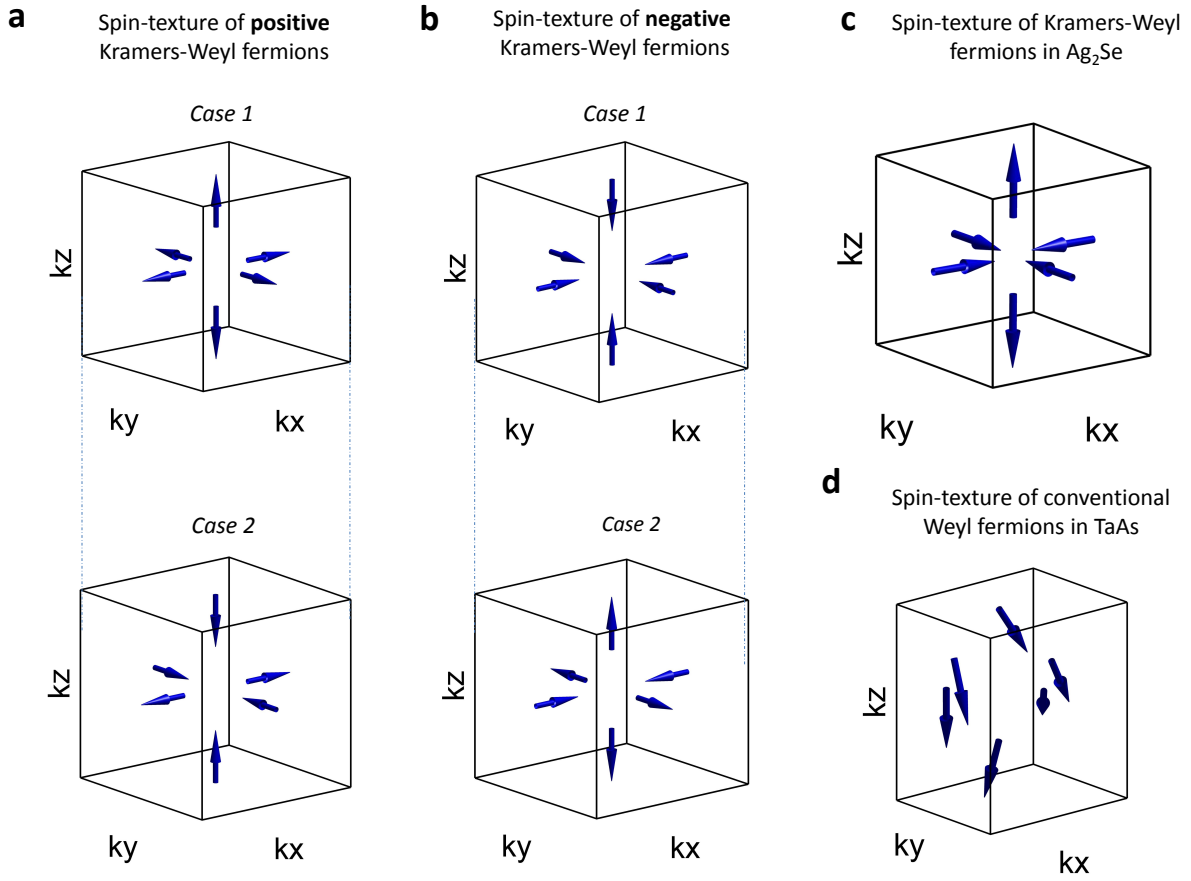


FIG. S10: **Spin-momentum locking of Kramers-Weyl fermions in the presence of rotational symmetries.** (a,b) The spin textures of Kramers-Weyl nodes with opposite chiral charges (c) The spin texture of Kramers-Weyl node in Ag_2Se near its Fermi level. (d) The spin texture of a conventional Weyl node in TaAs

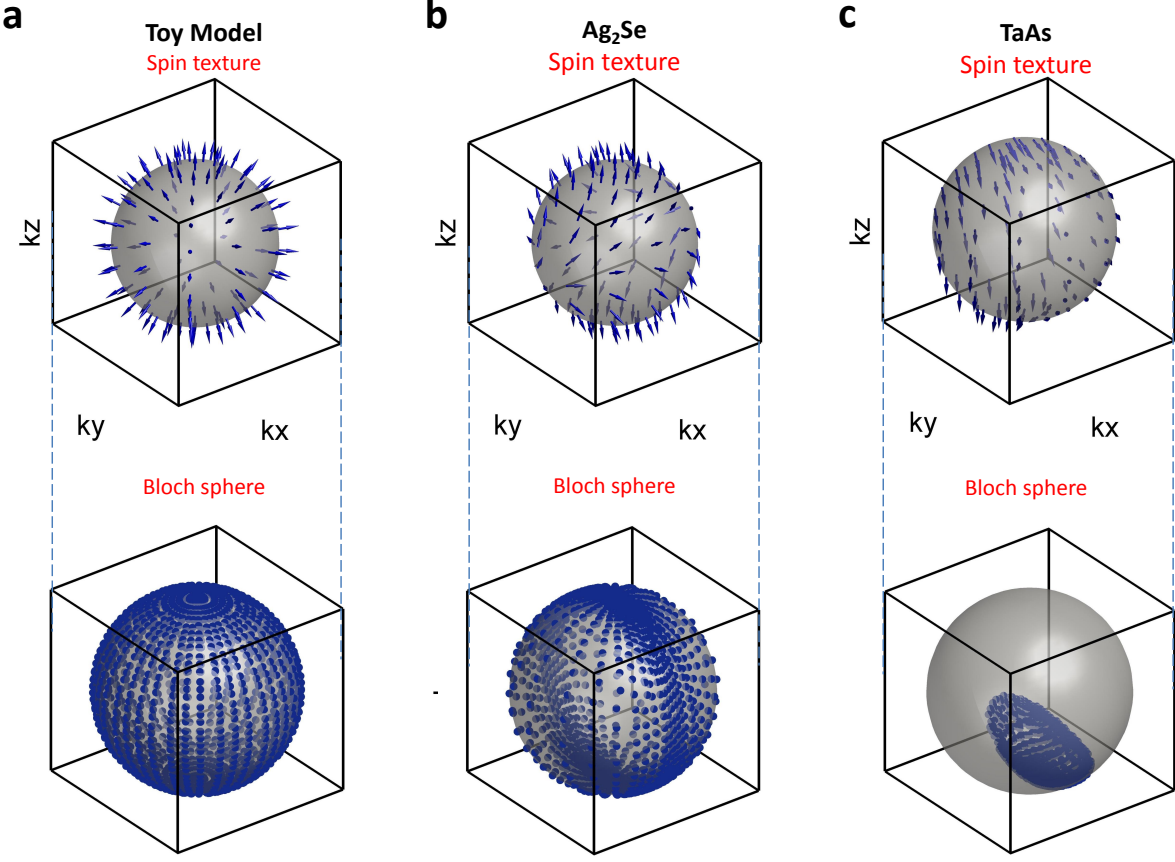


FIG. S11: **The spin textures of Kramers-Weyl fermions.** (a) **Top:** k space spin texture of the Kramers-Weyl fermion in a two-band toy-model. **Bottom:** The projection from the k space spin texture to a Bloch sphere. (b,c) The same as panel (a) but for Kramers-Weyl fermion in Ag_2Se and a conventional band-inversion induced Weyl fermion in TaAs

SI M. Calculated Spin Polarization near Kramers-Weyl Points

To demonstrate how the magnitude of the spin polarization but not the orientation is affected by inter-band couplings in Kramers-Weyl semimetals, consider the following model which pertains to bands at the Γ point of space group 16 or 19, for example

$$\mathcal{H}(\mathbf{k}) = \sum_{i=x,y,z} (v_i^{(0)} k_i \tau^0 \sigma^i + v_i^{(3)} k_i \tau^3 \sigma^i) + m \tau^z \sigma^0 + c \tau^y \sigma^z, \quad (\text{S16})$$

where the Pauli matrices σ^x , σ^y , σ^z as well as the identity matrix σ^0 act on the physical spin degree of freedom while the Pauli matrices τ^x , τ^y , τ^z as well as the identity matrix τ^0 act on an orbital degree of freedom, namely a doublet of an s and a p_z orbital. The model

respects C_2 symmetries around all three coordinate axes given by

$$\begin{aligned} C_2^x \mathcal{H}(k_x, k_y, k_z) (C_2^x)^{-1} &= \mathcal{H}(k_x, -k_y, -k_z), \\ C_2^y \mathcal{H}(k_x, k_y, k_z) (C_2^y)^{-1} &= \mathcal{H}(-k_x, k_y, -k_z), \\ C_2^z \mathcal{H}(k_x, k_y, k_z) (C_2^z)^{-1} &= \mathcal{H}(-k_x, -k_y, k_z), \end{aligned} \quad (\text{S17})$$

with $C_2^x = \tau^z \sigma^x$, $C_2^y = \tau^z \sigma^y$, and $C_2^z = \tau^0 \sigma^z$. In absence of spin-orbit coupling, only the parameter m in $\mathcal{H}(\mathbf{k})$ is nonzero and represents the energetic separation between the two orbital/bands. We want to study the limit where spin-orbit coupling is small compared to this parameter, i.e., $c \ll m$ and $\mathbf{v}^{(0)} \cdot \mathbf{k} \ll m$, $\mathbf{v}^{(3)} \cdot \mathbf{k} \ll m$.

At $\mathbf{k} = 0$, Hamiltonian (S16) has two distinct eigenvalues, each of which is two-fold degenerate. These two-fold degenerate subspaces are split linearly in \mathbf{k} at small finite \mathbf{k} . The possible spin polarization in each subspace follows from the spectrum of the spin operators $\tau^0 \sigma^x$, $\tau^0 \sigma^y$, and $\tau^0 \sigma^z$. They are given by

$$\begin{aligned} \tau^0 \sigma^x : &\quad \pm m/\sqrt{m^2 + c^2}, \\ \tau^0 \sigma^y : &\quad \pm m/\sqrt{m^2 + c^2}, \\ \tau^0 \sigma^z : &\quad \pm 1. \end{aligned} \quad (\text{S18})$$

We thus observe that the possible maximal spin polarization of these states (as they become nondegenerate at small finite \mathbf{k}) is reduced from 1 in the x and y direction due to the inter-band coupling c . Thus, if $m \gg c$, i.e., the bands are well separated on the scale of spin-orbit coupling, the spin polarization remains nearly perfect. This conclusion is independent of the presence of the rotational symmetries introduced above.

We also note that the direction (not the magnitude) of the spin polarization at finite \mathbf{k} away from TRIM points is constrained by the two-fold rotation symmetries. Let $|k_x, k_y, k_z\rangle$ be a nondegenerate eigenstate of the Hamiltonian. Then, for instance,

$$\langle k_x, 0, 0 | \tau^0 \sigma^y | k_x, 0, 0 \rangle = \langle k_x, 0, 0 | C_2^x \tau^0 \sigma^y (C_2^x)^{-1} | k_x, 0, 0 \rangle = -\langle k_x, 0, 0 | \tau^0 \sigma^y | k_x, 0, 0 \rangle = 0, \quad (\text{S19})$$

and by the same argument $\langle k_x, 0, 0 | \tau^0 \sigma^z | k_x, 0, 0 \rangle = 0$. Thus, the states along the k_x axis in the Brillouin zone can only have spin polarization in the x direction in spin space, those along the k_y axis can only have y polarization, and those along the k_z axis can only have z polarization. The only remaining freedom is whether the spin polarization in a given nondegenerate band is parallel or antiparallel to the coordinate axis. The spin structure on a

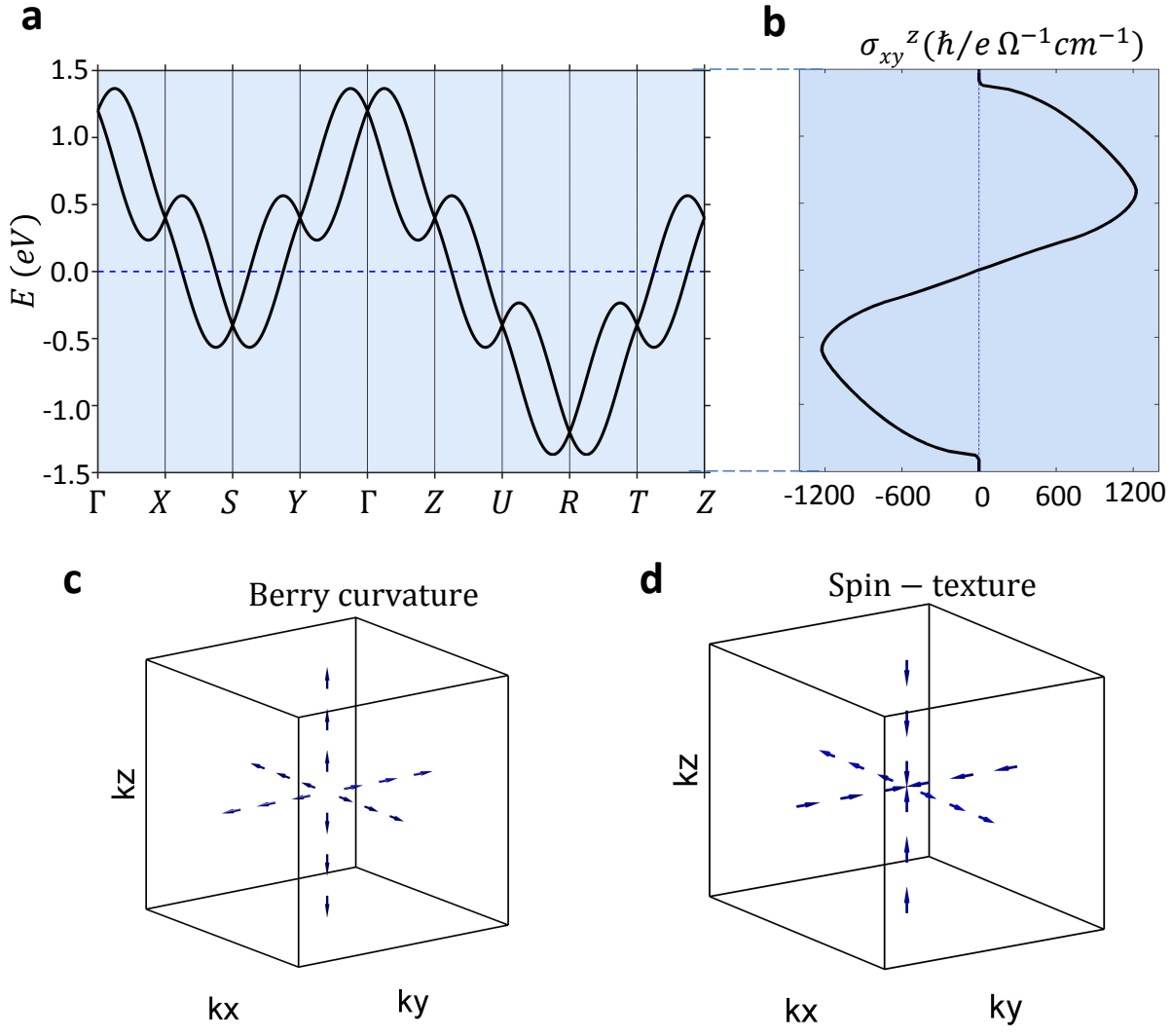


FIG. S12: **Spin Hall conductivity of Kramers-Weyl fermions**

spherical Fermi surface around the Weyl point can then take two qualitatively distinct forms (up to permutation of coordinate axes and global spin flips): Either the spin polarization is (anti-)parallel along all coordinate axes, or it has the opposite orientation along one axis with respect to the other two (e.g., parallel along one axis and antiparallel along the other two). Notice that the distinction between these two cases is not in one-to-one relation with the Chern number of the Fermi surface, since flipping the polarization along two coordinate axes (implemented by changing the sign of two of the v_i , $i = x, y, z$ parameters) does not change. To reach this conclusion, the presence of the three rotational symmetries introduced above is crucial.

Moreover, the real spin-momentum locking can lead to very large spin Hall conductivity.

Specifically, the spin Hall conductivity tensor is expressed as

$$\sigma_{\alpha\beta\gamma}^{\text{SpinHall}} = \int d^n \mathbf{k} f(\mathbf{k}) \Omega_{\beta\gamma}^\alpha$$

$$\Omega_{\beta\gamma}^\alpha = -2Im \sum_{n' \neq n} \frac{\langle n | \hat{J}_\beta^\alpha | n' \rangle \langle n | \hat{v}_\gamma | n' \rangle}{(E_n - E_{n'})^2}, \quad (\text{S20})$$

where α, β, γ can be any spatial direction, $f(\mathbf{k})$ is the Fermi-Dirac distribution function, $\Omega_{\beta\gamma}^\alpha$ is the spin Berry curvature, $\hat{J}_\beta^\alpha = \frac{1}{2}\{\hat{v}_\beta, \hat{s}_\alpha\}$, \hat{s} and \hat{v} are the spin and the velocity operators, $|n'\rangle$ is the n^{th} eigenvector. We calculate the a specific component of the spin Hall conductivity, $\sigma_{xyz}^{\text{SpinHall}}$ for the two-band Kramers-Weyl fermion model in the chiral space group 195 (P23). Fig. S12 shows the calculated $\sigma_{xyz}^{\text{SpinHall}}$ can be $1000 \frac{\hbar}{e} \Omega^{-1} \text{cm}^{-1}$. This is comparable to the value of the largest spin Hall materials such as the 5d transition metals (e.g., Pt). However, it is reasonable to presume that the charge conductivity is smaller than that of the metal Pt because of the smaller carrier numbers. Thus, we expect that the spin Hall angle ($\sigma^{\text{SpinHall}}/\sigma^{\text{charge}}$) can be even larger than that of Pt. In addition, the spin momentum locking suppresses scattering and thus enhances the spin life time and spin diffusion length.

SI N. Nonzero Chern Numbers of all Point Degeneracies in Chiral Crystals

Here, we further explore our finding that all point-like degeneracies in nonmagnetic chiral crystals with relevant SOC necessarily carry nontrivial Chern numbers. We first use symmetry and topology to place bounds on the set of allowed point degeneracies in these crystals, and then use Chern number calculations from this and previous works to exhaustively demonstrate that all of these points are necessarily topologically nontrivial.

In a generic 3D crystal, point degeneracies may occur at any point in the BZ; one may find them at high-symmetry points, along high-symmetry lines, in planes of the BZ, or at low-symmetry points throughout the 3D BZ. In Ref. [5], the authors demonstrated that all degeneracies in crystals with relevant SOC are either described by the corepresentations of the 230 \mathcal{T} -symmetric space groups, or are conventional $|C| = 1$ Weyl points. This implies that at any point in the BZ where bands are singly degenerate and there are no additional unitary crystal symmetries, the only degeneracies which may form are conventional Weyl fermions [18–20]. As the 65 chiral space groups necessarily do not contain reflection planes

(mirror or glide), as reflection is the operation of a twofold improper rotation $M_i = \mathcal{I} \times C_{2i}$ [1, 4], then unitary symmetries in chiral crystals are only present along high-symmetry lines and at high-symmetry points in the BZ. Therefore, we need only demonstrate the nontrivial Chern numbers of point-like degeneracies that are either characterized by a two- (or higher-) dimensional corepresentation at a high-symmetry point, or are characterized by the crossing of two different corepresentations along a high-symmetry line.

We begin by enumerating the allowed point-like degeneracies in chiral crystals at high-symmetry BZ points. Following the analysis performed in Ref. [11] for crystals with negligible SOC, the authors of Ref. [21] discovered that several of the high-fold-degenerate unconventional fermions, such as the threefold-degenerate so-called “spin-1 Weyl points” at the P point in SG 214 and the double spin-1 Weyl points at the R point in SG 198 $P2_13$, carry nontrivial Chern numbers. When the results of that work are combined the recent results of Refs. [5, 17, 22, 23] and our findings in this work, we conclude that all of the point-like degeneracies at high-symmetry points in nonmagnetic chiral crystals with relevant SOC exhibit nontrivial Chern numbers, and are either (double) spin-1 Weyl fermions, chiral spin-3/2 fermions, or Kramers-Weyl fermions.

Along high-symmetry lines in 3D SGs with \mathcal{T} -symmetry, bands may only cross to form two-, three-, or fourfold degeneracies [1, 4, 22]. Of these, the threefold-degenerate crossings require mirror symmetry [24–26], and thus may only occur in achiral space groups. Furthermore, it was demonstrated in Refs. [6, 7, 27, 28] that all twofold point degeneracies along high-symmetry lines are either single-, double-, or triple-Weyl fermions. Therefore, the only remaining possibilities are the fourfold point-like degeneracies allowed along the BZ edges in chiral space groups with two or more orthogonal screw symmetries [15, 16]. By exhaustively considering all of the corepresentations present along zone-edge lines in these SGs [5, 22], we find that these fourfold degeneracies come in two categories. Whether they are filling-enforced [4, 14, 17] (for example, in SGs 19 $P2_12_12_1$ and 198 $P2_13$), or formed from band inversion (for example, in SGs 18 $P2_12_12$ and 90 $P42_12$), they are locally described by $k \cdot p$ theories with either a twofold or a fourfold rotation axis, as well as the combined antiunitary symmetry $\bar{\mathcal{T}}$ of twofold screw rotation and time-reversal, where $\bar{\mathcal{T}}^2 = -1$ along the zone-edge line. We find that all of these fourfold degeneracies carry nontrivial Chern numbers. Fourfold-degenerate chiral fermions with twofold rotation axes appear in our model of SG 19 in SI F, and can also be obtained by stacking and inverting copies of the 2D model in Ref. [4]

of layer group 21, which is isomorphic to SG 18 modulo translations. This model can then also be tuned to a C_4 -symmetric limit to realize fourfold-degenerate chiral fermions with fourfold rotation axes. A more detailed discussion of these fourfold-degenerate, zone-edge chiral fermions recently appeared in Ref. [16].

The nodal degeneracies discussed here comprise all of the possible point-like nodal degeneracies in nonmagnetic chiral crystals with relevant SOC; as they all manifestly exhibit nontrivial Chern numbers, *all* point-like degeneracies in these crystals are necessarily topologically nontrivial.

SI O. Comparison between Kramers-Weyl Fermions and Other Chiral Fermions

It is important to highlight that in the context of symmetry and topology, Kramers-Weyl fermions are distinct from previous examples of chiral fermions. Conventional band-inversion Weyl semimetals [18–20, 29–31] are not guaranteed by general symmetry criteria, but rather form as the result of favorable energetics. Furthermore, in many of the conventional Weyl semimetals proposed to date, the degree of band inversion is quite small, and is thus subject to the uncertainties of computational and experimental parameters. Unconventional high-fold chiral fermions [11, 17, 21, 23] are protected by highly specific combinations of crystal symmetries, and are thus susceptible to perturbations that break the exact crystal symmetries of their SGs [32]. Kramers-Weyl fermions, conversely, are neither generated by a band inversion, nor are dependent on specific combinations crystal symmetries; they are guaranteed to exist, and to be chiral fermions, merely by the action of \mathcal{T} symmetry on the irreducible representations of the chiral point groups. Moreover, as $|C| = 1$ Weyl fermions, they can only be destroyed through pairwise annihilation, which may only occur under a large magnetic field that moves them far off from the TRIMs, or through the zone-folding effects of commensurate spin- or charge-density waves. Thus, Kramers-Weyl fermions are much more robust against perturbations than other chiral fermions.

[1] Bradley, C. J. & Cracknell, A. P. *The Mathematical Theory of Symmetry in Solids*. Clarendon Press Oxford, Oxford, UK, 1972.

- [2] Juan, F. d. et al. Quantized circular photogavanic effect in Weyl semimetals, *Nat. Commun.* **8**, 15995 (2017).
- [3] Belinicher, V. I. & Sturman, A. G., The photogalvanic effect in media lacking a center of symmetry, *Physics Uspekhi* **23**, 199-223 (1980).
- [4] Wieder, B.J. & Kane, C.L., Spin-orbit semimetals in the layer groups. *Phys. Rev. B* **94**, 155108 (2016).
- [5] Bradlyn, B. et al. Topological quantum chemistry. *Nature* **547**, 298 (2017).
- [6] Tsirkin, S. S., Souza, I. & Vanderbilt, D. Composite Weyl nodes stabilized by screw symmetry with and without time-reversal invariance, *Phys. Rev. B* **96**, 045102 (2017).
- [7] Fang, C. et al. Multi-Weyl topological semimetals stabilized by point group symmetry. *Phys. Rev. Lett.* **107**, 127205 (2011).
- [8] Young, S. M. et al. Dirac semimetal in three dimensions. *Phys. Rev. Lett.* **108**, 140405 (2012).
- [9] Wieder, B. J. et al. Wallpaper fermions and the nonsymmorphic Dirac insulator, *Science*, **316**, 245-251 (2018).
- [10] Xiao, M. & Fan, S. Topologically charged nodal surface. Preprint at <https://arxiv.org/abs/1709.02363> (2017).
- [11] Mañes, J. L. Existence of bulk chiral fermions and crystal symmetry, *Phys. Rev. B* **85**, 155118 (2012).
- [12] Bouhon, A. and Black-Schaffer, A. M. Global band topology of simple and double Dirac-point semimetals. *Phys. Rev. B* **95**, 241101(R) (2017).
- [13] Geilhufe, R. M., Borysov, S. S., Bouhon, A., & Balatsky, A. V. Data mining for three-dimensional organic Dirac materials: focus on space group 19. *Sci. ReP.* **7**, 7298 (2017).
- [14] Watanabe, H. et al. Filling constraints for spin-orbit coupled insulators in symmorphic and nonsymmorphic crystals. *Proc. Natl. Acad. Sci.* **112**, 14551-14556 (2015).
- [15] Bradlyn, Barry. *Private Communication* (2018).
- [16] Flicker, F., de Juan, F., Bradlyn, B., Morimoto, T., Vergniory, M. G., & Grushin, A. Preprint at <https://arxiv.org/abs/1806.09642> (2018).
- [17] Chang, G. et al. Unconventional chiral fermions and large topological fermi arcs in RhSi. *Phys. Rev. Lett.* **119**, 206401 (2017).
- [18] Murakami, S. Phase transition between the quantum spin Hall and insulator phases in 3D: emergence of a topological gapless phase. *New J. Phys.* **9**, 356 (2007).

- [19] Wan, X. et al. Topological semimetal and Fermi-arc surface states in the electronic structure of pyrochlore iridates. *Phys. Rev. B* **83**, 205101 (2011).
- [20] Burkov, A. A. & Balents, L. Weyl Semimetal in a Topological Insulator Multilayer. *Phys. Rev. Lett.* **107**, 127205 (2011).
- [21] Bradlyn, B. et al. Beyond Dirac and Weyl fermions: Unconventional quasiparticles in conventional crystal. *Science* **353**, aaf5037 (2016).
- [22] Elcoro, L. et al. Double crystallographic groups and their representations on the Bilbao Crystallographic Server. *J. Appl. Cryst.* **50**, 1457 (2017).
- [23] Tang, P., Zhou, Q. & Zhang, S.-C. Multiple types of topological fermions in transition metal silicides. *Phys. Rev. Lett.* **119**, 206402 (2017).
- [24] Weng, H. M., Fang C., Fang, Z., & Dai, X. *Phys. Rev. B* **93**, 241202(R) (2016).
- [25] Zhu, Z., Winkler, G. W., Wu, Q. S., Li, J. and Soluyanov, A. A. *Phys. Rev. X* **6**, 031003 (2016).
- [26] Chang, G. et al. *Sci. Rep.* **7**, 1688 (2017).
- [27] Xu, G., Weng, H., Wang, Z., Dai, X., & Fang, Z. Chern Semimetal and the Quantized Anomalous Hall Effect in HgCr_2Se_4 . *Phys. Rev. Lett.* **107**, 186806 (2011).
- [28] Huang, S.-M. et al. New Type of Weyl Semimetal with Quadratic Double Weyl Fermions. *Proc. Natl. Acad. Sci.* **113**, 1180-1185 (2016).
- [29] Xu, S.-Y. et al. Discovery of a Weyl Fermion semimetal and topological Fermi arcs. *Science* **349**, 613-617 (2015).
- [30] Lv, B. Q. et al. Experimental discovery of Weyl semimetal TaAs. *Phys. Rev. X* **5**, 031013 (2015).
- [31] Yang, L. X. et al. Weyl semimetal phase in the non-centrosymmetric compound TaAs. *Nat. Phys.* **11**, 728-732 (2015).
- [32] Wieder, B. J. et al. Double dirac semimetals in three dimensions. *Phys. Rev. Lett.* **116**, 186402 (2016).